

# The Birth of a Galaxy. II. The Role of Radiation Pressure

John H. Wise<sup>1\*</sup>, Tom Abel<sup>2</sup>, Matthew J. Turk<sup>3</sup>, Michael L. Norman<sup>4</sup> and Britton D. Smith<sup>5</sup>

<sup>1</sup> *Center for Relativistic Astrophysics, Georgia Institute of Technology, 837 State Street, Atlanta, GA 30332, USA*

<sup>2</sup> *Kavli Institute for Particle Astrophysics and Cosmology, Stanford University, Menlo Park, CA 94025, USA*

<sup>3</sup> *Department of Astronomy, Columbia University, 538 West 120th Street, New York, NY 10027, USA*

<sup>4</sup> *Center for Astrophysics and Space Sciences, University of California at San Diego, La Jolla, CA 92093, USA*

<sup>5</sup> *Department of Physics & Astronomy, Michigan State University, East Lansing, MI 48824, USA*

21 May 2018

## ABSTRACT

Massive stars provide feedback that shapes the interstellar medium of galaxies at all redshifts and their resulting stellar populations. Here we present three adaptive mesh refinement radiation hydrodynamics simulations that illustrate the impact of momentum transfer from ionising radiation to the absorbing gas on star formation in high-redshift dwarf galaxies. Momentum transfer is calculated by solving the radiative transfer equation with a ray tracing algorithm that is adaptive in spatial and angular coordinates. We find that momentum input partially affects star formation by increasing the turbulent support to a three-dimensional rms velocity equal to the circular velocity of early haloes. Compared to a calculation that neglects radiation pressure, the star formation rate is decreased by a factor of five to  $1.8 \times 10^{-2} M_{\odot} \text{ yr}^{-1}$  in a dwarf galaxy with a dark matter and stellar mass of  $2.0 \times 10^8 M_{\odot}$  and  $4.5 \times 10^5 M_{\odot}$ , respectively, when radiation pressure is included. Its mean metallicity of  $10^{-2.1} Z_{\odot}$  is consistent with the observed dwarf galaxy luminosity-metallicity relation. However, what one may naively expect from the calculation without radiation pressure, the central region of the galaxy overcools and produces a compact, metal-rich stellar population with an average metallicity of  $0.3 Z_{\odot}$ , indicative of an incorrect physical recipe. In addition to photo-heating in H II regions, radiation pressure further drives dense gas from star forming regions, so supernovae feedback occurs in a warmer and more diffuse medium, launching metal-rich outflows. Capturing this aspect and a temporal separation between the start of radiative and supernova feedback are numerically important in the modeling of galaxies to avoid the “overcooling problem”. We estimate that dust in early low-mass galaxies is unlikely to aid in momentum transfer from radiation to the gas.

**Key words:** cosmology — methods: numerical — hydrodynamics — radiative transfer — star formation

## 1 INTRODUCTION

Stellar radiation from massive stars and their supernova (SN) explosions significantly alter the surrounding interstellar medium (ISM) and, thus, subsequent star formation in the host galaxy (for a review, see McKee & Ostriker 2007). On a grander scale, their input can drive large-scale outflows that increase the entropy and metallicity of the intergalactic medium (Davies et al. 1998; Aguirre et al. 2001a; Benson 2010, for a review). To date, the primary feedback mechanism in galaxy formation simulations originate from SNe,

which is implemented by locally injecting thermal and kinetic energy and metals (Cen & Ostriker 1992). There are various relevant physics, such as photoheating (e.g. Gnedin 2000), momentum input from radiation (e.g. Haehnelt 1995), cosmic rays (e.g. Jubelgas et al. 2008), and magnetic fields (e.g. Wang & Abel 2009; Kotarba et al. 2011), that can play an important role in star and galaxy formation. Numerical simulations are a useful tool in exploring the impacts of these physical processes in galaxy formation. But only recently, feedback mechanisms other than SNe have begun to appear in cosmological simulations, sometimes in a phenomenological manner, because of resolution and algorithmic limitations.

\* e-mail: jwise@physics.gatech.edu

Simulating the first low-mass galaxies with the correct physical model is crucial because they are the building blocks for all subsequent galaxies, and it is clear that stellar radiation from them were predominately responsible for reionisation (e.g. Shapiro 1986; Fan, Carilli & Keating 2006; Bouwens et al. 2011). The most luminous of these “reionisers” have been detected at  $6 < z < 10$  in the *Hubble Ultra Deep Field* (HUDF) and from ground-based campaigns (e.g. Bouwens et al. 2008; McLure et al. 2010; Finkelstein et al. 2010; Ouchi et al. 2010). Even lower mass and higher redshift galaxies will be detected with the *Atacama Large Millimeter Array* (ALMA) and the *James Webb Space Telescope* (JWST), providing additional constraints on early galaxy formation, reionisation, and the early metal enrichment of the intergalactic medium. Closer to home, nearby dwarf galaxies provide clues to their formation, where all of them formed stars at or before reionisation (Grebel, Gallagher & Harbeck 2003), in their  $[\alpha/\text{Fe}]$  versus  $[\text{Fe}/\text{H}]$  evolution (Tolstoy, Hill & Tosi 2009), metallicity distribution functions (Kirby et al. 2011), metallicity radial gradients (Tolstoy et al. 2004), star formation histories (Monelli et al. 2010), and individual abundance patterns (Frebel et al. 2010; Caffau et al. 2011). These data from the high-redshift and the local universe provide important constraints on numerical models of star formation and feedback.

The first generation of galaxies with  $10^8 \lesssim M_{\text{halo}}/M_{\odot} \lesssim 10^{10}$  (Bromm & Yoshida 2011) are an excellent cosmological testbed to numerically investigate the impact of each physical process. Compared to simulating larger galaxies, they present a relatively clean scenario with few instances of prior star formation that sets the “initial conditions” for galaxy formation. They are also small enough so it is computationally feasible to achieve high enough resolution to well resolve star forming regions. Their progenitors may have hosted several metal-free and massive (Pop III) stars, enriching the IGM and pre-heating the gas to thousands of degrees, which then re-accretes into the dark matter (DM) halo and forms a dwarf galaxy (Wise & Abel 2008; Greif et al. 2010). In this paper, we investigate the impact of radiative cooling from metals and a  $\text{H}_2$ -dissociating radiation background, but the main focus of this work is the effect of momentum transfer from ionising radiation, i.e. *radiation pressure*, on star formation in such galaxies.

Regulating star formation by radiation pressure is not a new idea, especially in the Milky Way and present-day star formation (Shu et al. 1991; Ferrara 1993; Li & Shu 1996; Matzner & McKee 1999). However, Haehnelt (1995) was the first to apply this idea to galaxy formation. He found that radiation pressure could be the dominant feedback process within  $\sim 110$  pc in DM haloes with masses  $\lesssim 10^9 - 10^{10} M_{\odot}$ . He suggested that it could be more important than SNe heating in driving outflows from such early dwarf galaxies. In turn, this would lower their gas fractions and alter their predicted mass-to-light ratios. In larger galaxies, it was unclear whether momentum deposition could drive outflows through ionising radiation alone. However, UV radiation can be absorbed by dust and be re-emitted many times, increasing the momentum transfer to the absorber. Without making the assumption that gas dynamics are coupled to dust grains, radiation pressure from massive stars were found to drive dust outflows

in cosmological simulations, enriching the IGM to the C and Si abundances found in  $z = 3$  quasar absorption lines (Aguirre et al. 2001a,b,c). Murray, Quataert & Thompson (2005) and Thompson, Quataert & Murray (2005) investigated the effects of radiation pressure in driving galactic outflows from starburst galaxies and regulating star formation by reducing the gas supply for further star formation and BH growth. They found that it could explain the  $M_{\text{BH}} - \sigma$  relation for early-type galaxies, where  $\sigma$  is the stellar velocity dispersion (Ferrarese & Merritt 2000; Gebhardt et al. 2000; Tremaine et al. 2002). They also found that momentum-driven winds could be launched if the opacity  $\kappa \gtrsim 6 \text{ cm}^2 \text{ g}^{-1}$  in a starburst galaxy, assuming that momentum transfer is increased by a factor of  $\tau_{\text{IR}} - 1$ , where  $\tau_{\text{IR}}$  is the optical depth in the infrared (IR).

These works led to various implementations of momentum transfer in numerical studies of galaxy formation, usually in the form of “kicking” particles with some wind velocity from star-forming regions (e.g. Springel & Hernquist 2003; Oppenheimer & Davé 2008; Sales et al. 2010; Hopkins, Quataert & Murray 2011). The early implementations decoupled these wind particles from the hydrodynamics to create outflows; otherwise, they would be confined to the galaxy. Recently, Krumholz & Thompson (2012) investigated the parsec-scale effects of momentum transfer in radiation hydrodynamics simulations and compared them to the aforementioned subgrid models. They found that most of the radiation is not trapped because the optically-thick shell breaks up from a radiation Rayleigh-Taylor instability, i.e. momentum transfer does not scale as  $\tau_{\text{IR}}$ . This may lead to an overestimate of momentum transfer in the subgrid models when the radiation source shines above 10 per cent of its Eddington limit.

Here we present results that demonstrate the effects of momentum transfer from ionising radiation on dwarf galaxy formation, using cosmological radiation hydrodynamics simulations. The amount of momentum deposition is directly calculated from our radiation transport solver ENZO+MORAY (Wise & Abel 2011). In the next section, we outline some analytics that govern the dynamics of outflows and turbulence created by radiation pressure. Then in Sec. 3, we describe the numerical simulation setup and algorithms. In Sec. 4, we present the effects of radiation pressure on star formation and metal enrichment in dwarf galaxies, preventing the overcooling problem seen often in galaxy formation simulations. We discuss possible constraints on high-redshift dwarf galaxies and then focus on differences in feedback implementations in simulations in Sec. 5. We finish that section with an estimate of momentum transfer onto dust grains in dwarf galaxies. We summarise our findings in Sec. 6.

## 2 MOMENTUM TRANSFER FROM IONISING RADIATION

First we review some basic analytical arguments on momentum transfer from ionising radiation. We take a similar approach as Haehnelt (1995) and Murray, Quataert & Thompson (2005) and use an Eddington-like argument on an entire galaxy, equating the radiation pressure from ionising stellar radiation to the gravitational potential of the host dark matter halo.

Its application to local star formation and feedback has been extensively studied (McKee & Ostriker 2007, and references therein). But can we apply the same principles to an entire dwarf galaxy? How will the energetics differ if the momentum transfer originates from ionising radiation instead of protostellar winds or Thomson scattering?

In the traditional Eddington approach (Eddington 1926), Thomson scattering is the source of radiation pressure. The Eddington luminosity limit is

$$L_{\text{edd}} = \frac{4\pi GMm_p c}{\sigma_T}, \quad (1)$$

where  $M$  is the mass of object,  $m_p$  is the proton mass, and  $\sigma_T = 6.65 \times 10^{-25} \text{ cm}^2$  is the Thomson cross-section. However, the absorption cross-section for hydrogen  $\sigma_{\text{HI}} = 6.35 \times 10^{-18} \text{ cm}^2$  at 1 Ryd, which is  $\sim 10^7$  times larger than the Thomson cross-section. However, it should be noted that a spectrum-weighted cross-section is somewhat lower because  $\sigma_{\text{HI}} \propto \nu^{-3}$ . Thus momentum transfer during the absorption of ionising photons might significantly affect the large-scale dynamics in the galaxy.

For illustrative purposes, we focus on a single expanding H II region with hydrogen only that is embedded in a DM halo. A shock front forms at the edge of the H II region as when the ionisation front becomes D-type (Osterbrock 1989), i.e., the expansion speed of the H II region slows below the sound speed of the ionised medium. If the ionisation front coincides with the shock front, the optical depth from the radiation source will exceed unity within the shock. We can simplify the calculation by assuming that the H II region is optically thin and all of the ionising radiation momentum is transferred to the optically-thick shock.

Murray, Quataert & Thompson (2005) considered the spherically symmetric and self-gravitating case where the stellar system is contained within a halo with a gas fraction  $f_{\text{gas}}$ . Their main focus was on nuclear starbursts and the resulting outflows and explaining the  $M - \sigma$  relationship (Ferrarese & Merritt 2000; Gebhardt et al. 2000; Tremaine et al. 2002). They neglected thermal pressure forces from the H II region because it is negligible for a stellar system that is centered in the gravitational potential of halos that host  $L \gtrsim L^*$  galaxies. For a central ionising luminosity  $L$  where each photon is absorbed once, the momentum equation is

$$\frac{dP}{dt} = -\frac{GM(r)M_{\text{gas}}(r)}{r^2} + \frac{L}{c}. \quad (2)$$

In the case where photons are absorbed and re-emitted many times in a dusty medium, the second term can become important. Murray, Quataert & Thompson showed that for a luminosity  $L \gtrsim 4f_{\text{gas}}\sigma^4 c/G$ , the gas moves outward driven by pure radiation pressure, where  $\sigma$  is the halo velocity dispersion and all radiation is assumed to be absorbed.

For a dwarf galaxy with  $\sigma = 20 \text{ km s}^{-1}$  and the cosmic baryon fraction, this critical luminosity is on the order of  $10^{42} \text{ erg s}^{-1}$  ( $10^{8.4} L_{\odot}$ ), equivalent to a mass-to-light ratio on the order of unity for a Salpeter IMF. The gravitational potential in dwarf galaxies with  $V_c \lesssim 30 \text{ km s}^{-1}$  cannot prevent the expansion of the dense shell surrounding H II regions into the IGM. Furthermore, star formation is not necessarily concentrated in the centre of these small irregular galaxies (Tolstoy, Hill & Tosi 2009). If the H II region is pressure-supported (e.g., see Ferrara 1993), then we

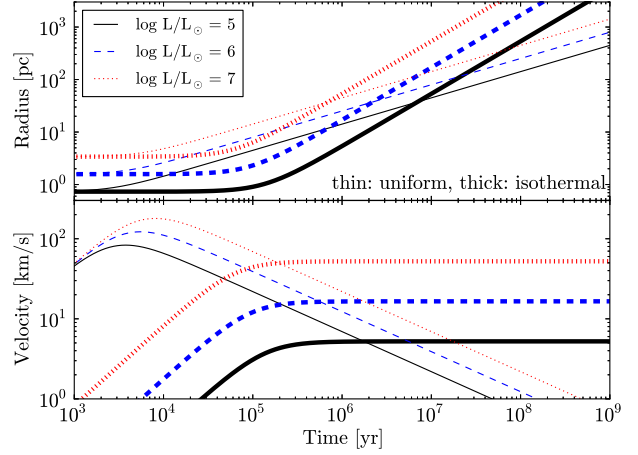


**Figure 1.** Radius (top) and velocity (bottom) of an expanding optically thick shell driven by momentum transfer from ionising radiation for a central luminosity of  $L = 10^5, 10^6, 10^7 L_{\odot}$  with an average ionising photon energy of 20 eV.

can neglect the gravitational force term in Eq. 2. Taking  $L$  to be time-independent and instantaneously non-zero at  $t > 0$ , the momentum equation for the optically-thick shell is simply  $P(t) = Lt/c$ . We consider the spherically-symmetric case where the shell sweeps all of the ISM with a density  $\rho = \rho(r)$  in its path, and it moves at a velocity

$$v(t) = \frac{Lt}{cM_{\text{shell}}} = \frac{Lt}{c} \left[ 4\pi \int_0^r r'^2 \rho(r') dr' \right]^{-1}. \quad (3)$$

Solving for radius and velocity with a homogeneous medium  $\rho(r) = \rho_0$  and isothermal density profile  $\rho(r) = \rho_0(r/r_0)^{-2}$ , we obtain

$$r(t) = \begin{cases} (r_i^4 + 2At^2)^{1/4} & (\rho = \rho_0) \\ (r_i^2 + At^2/3r_0^2)^{1/2} & (\rho \propto r^{-2}) \end{cases} \quad (4)$$

$$v(t) = \begin{cases} tA(r_i^4 + 2At^2)^{-3/4} & (\rho = \rho_0) \\ t(A/3r_0^2)(r_i^2 + At^2/3r_0^2)^{-1/2} & (\rho \propto r^{-2}) \end{cases}, \quad (5)$$

where  $A \equiv 3L/4\pi\rho_0 c$ , and  $r_i$  is the radius where the optically thick shell first forms. The initial Strömngren sphere radius is calculated by equating the ionising photon luminosity  $\dot{N}_{\gamma} = L/\langle E_{\gamma} \rangle$  to the number of recombinations, so that

$$r_i = \left( \frac{3\dot{N}_{\gamma}}{4\pi n_0^2 \alpha_B} \right)^{1/3}, \quad (6)$$

given an initial absorber number density  $n_0$  of the star-forming region. Here  $\langle E_{\gamma} \rangle$  is the average ionising photon energy, and  $\alpha_B \approx 2.5 \times 10^{-13} \text{ cm}^3 \text{ s}^{-1}$  is the Case B recombination rate at  $T = 10^4 \text{ K}$ . Molecular complexes are very clumpy and, in the Galactic plane, they have an average density in the range of  $10^2 - 10^4 \text{ cm}^{-3}$  (Bergin & Tafalla 2007). For a representative stellar cluster,

$$r_i = 1.57 L_6^{1/3} E_{\gamma,20}^{-1/3} n_3^{-1/3} \text{ pc}, \quad (7)$$

where  $L_6 = L/10^6 L_{\odot}$ ,  $E_{\gamma,20} = E_{\gamma}/20 \text{ eV}$ , and  $n_3 = n_0/10^3 \text{ cm}^{-3}$ . We plot  $r(t)$  and  $v(t)$  for  $L = 10^5, 10^6, 10^7 L_{\odot}$ ,  $\rho_0 = 1 \text{ cm}^{-3}$ , and  $\langle E_{\gamma} \rangle = 20 \text{ eV}$  in Figure 1 for a uniform and an isothermal density profile. We set  $r_0 = 15 \text{ pc}$

so that both the uniform and isothermal sphere with radius  $3r_0$  contains  $10^4 M_\odot$ . In a uniform medium, the shell rapidly accelerates to its maximum velocity  $\sim 100 \text{ km s}^{-1}$  after  $10^4 \text{ yr}$ . Its velocity decreases as the shell accumulates material from the ISM. It eventually reaches 1 kpc after 1 Gyr for the  $10^6 L_\odot$  case. In the isothermal sphere, the shell accelerates as it runs down the density slope, reaching 1 kpc after 50 Myr. The shell reaches a constant velocity  $v_s = (L/4\pi\rho_0 cr_0^2)^{1/2} \sim 13L_6 \text{ km s}^{-1}$  after about a Myr (Bally & Lada 1983; Shu et al. 1991; Matzner & McKee 1999) with a fraction  $f = 5.0 \times 10^{-4} L_6^{-0.5}$  of the radiation energy being transferred to the kinetic energy of the shell.

This ideal model will break down as the shell when gravitational forces from the DM halo becomes larger than  $L/c$  and the thermal pressure inside the H II region. However if parts of the shell fragment because of ionisation front or thin-shell instabilities, the diffuse gas in the openings of the shell will experience a greater acceleration, i.e. champagne flows (e.g. Yorke, Tenorio-Tagle & Bodenheimer 1983). These radiation pressure driven champagne flows are a possible mechanism for enhancing mass outflow velocities in dwarf galaxies in this model.

The terminal velocity for the shell traveling down a  $r^{-2}$  density profile is comparable to the circular velocity of the DM halo. Radiative pressure driven winds in dwarf galaxies may contribute more to the driving of turbulence instead of outflows when the shells are contained within the halo. Collisions between surviving swept-up shells can drive turbulence in the star-forming region. This has been shown to be likely in present-day star formation (e.g. Norman & Silk 1980; Franco 1983; Krumholz, Matzner & McKee 2006; Matzner 2007). This added turbulent support may help in regulating star formation by preventing a catastrophic central collapse in a galaxy.

We can understand the evolution of turbulence by investigating the vorticity equation,

$$\frac{D\boldsymbol{\omega}}{Dt} = -\boldsymbol{\omega}\nabla \cdot \mathbf{v} - \frac{\nabla\mathcal{P} \times \nabla\rho}{\rho^2} + \nu\nabla^2\boldsymbol{\omega}, \quad (8)$$

where  $D/Dt$  is the fluid derivative,  $\mathcal{P}$  is pressure, and  $\nu$  is the viscosity. In our analysis, we consider non-viscous fluids and set  $\nu = 0$ . The first term describes the stretching of vorticity; the second term comes from non-barotropic flows, i.e.  $\mathcal{P} \neq \mathcal{P}(\rho)$ , and the last term accounts for the dissipation of turbulence through viscous forces. Non-barotropic flows occur at and near shock fronts and have been found to be the main process that sustains vorticity in several situations. For example, virial shocks and internal weak shocks have been found to drive turbulence during halo virialization (Wise & Abel 2007a; Greif et al. 2008). Furthermore, non-thermal pressure, such as radiation pressure or cosmic rays, contributes to the generation of vorticity when its gradient (acceleration) is not aligned with the density gradient. To determine the importance of radiation pressure in outflows and sustaining turbulent motions, we use cosmological radiation hydrodynamics simulations that focus on dwarf galaxy formation, which we describe next.

### 3 COSMOLOGICAL SIMULATIONS

We expand upon the simulation presented in Wise et al. (2012, hereafter Paper I) that focused on the transition from Population III to II star formation and the effects of radiative and supernova feedback on early dwarf galaxy formation. In this work, we compare two new simulations that add radiative cooling from metals, an H<sub>2</sub>-dissociating radiation background, and momentum transfer from ionising radiation to the original physics set. These simulations were run with the adaptive mesh refinement (AMR) code ENZO v2.0<sup>1</sup> (Bryan & Norman 1997; O’Shea et al. 2004). It uses an  $N$ -body adaptive particle-mesh solver (Efsthathiou et al. 1985; Couchman 1991; Bryan & Norman 1997) to follow the DM dynamics. It solves the hydrodynamical equation using the second-order accurate piecewise parabolic method (Woodward & Colella 1984; Bryan et al. 1995), while a Riemann solver ensures accurate shock capturing with minimal viscosity. We use the recently added HLLC Riemann solver (Toro, Spruce & Speares 1994) for additional stability in strong shocks and rarefaction waves.

We use a simulation box of 1 Mpc on a side with a base resolution of  $256^3$ , resulting in a DM mass resolution of  $1840 M_\odot$ . This allows us to resolve  $2 \times 10^5 M_\odot$  DM haloes that can cool by H<sub>2</sub> in the gas phase (Tegmark et al. 1997) by at least 100 particles. We refine the grid on baryon overdensities of  $3 \times 2^{-0.2l}$ , where  $l$  is the AMR level, resulting in a super-Lagrangian behaviour (also see O’Shea & Norman 2008). We also refine on a DM overdensity of three and always resolve the local Jeans length by at least 4 cells, avoiding artificial fragmentation during gaseous collapses (Truelove et al. 1997). If any of these criteria are met in a single cell, it is flagged for further spatial refinement.

We initialise the simulations with GRAFIC (Bertschinger 2001) at  $z = 130$  and use the cosmological parameters from the 7-year WMAP  $\Lambda$ CDM+SZ+LENS best fit (Komatsu et al. 2011):  $\Omega_M = 0.266$ ,  $\Omega_\Lambda = 0.734$ ,  $\Omega_b = 0.0449$ ,  $h = 0.71$ ,  $\sigma_8 = 0.81$ , and  $n = 0.963$  with the variables having their usual definitions. We use a maximum refinement level of  $l = 12$ , resulting in a maximal comoving resolution of 1 pc. We do not smooth the DM mass field at any level, which is done to reduce artificial gas heating from DM particles in simulations that have regions that are baryon dominated (e.g. Abel, Bryan & Norman 2002). The adaptive particle-mesh solver has a force resolution of two cell widths of a given AMR grid. We compare the simulations at  $z = 8.1$ , which is when the metal cooling simulation reaches an ionised volume fraction of 96 percent.

#### 3.1 Star formation

We distinguish Pop II and Pop III SF by the total metallicity of the densest cell in the molecular cloud. Pop II stars are formed if  $[Z/H] > -4$ , and Pop III stars are formed otherwise. We do not consider hypothetical Pop III.2 stars or intermediate mass stars from CMB-limited cooling. Here we outline how we treat Pop II and III SF in our simulations; for more details and justifications, we refer the reader to Wise et al. (2012).

<sup>1</sup> [enzo.googlegcode.com](http://enzo.googlegcode.com), changeset 03a72f4f189a

### 3.1.1 Population III star formation

We use the same Pop III SF model as Wise & Abel (2008) where each star particle represents a single star. In this model, a star particle forms when a cell has all of the following criteria:

- (i) an overdensity of  $5 \times 10^5$  ( $\sim 10^3 \text{ cm}^{-3}$  at  $z = 10$ ),
- (ii) a converging gas flow ( $\nabla \cdot \mathbf{v}_{\text{gas}} < 0$ ), and
- (iii) a molecular hydrogen fraction  $f_{\text{H}_2} > 5 \times 10^{-4}$ .

These physical conditions are typical of collapsing metal-free molecular clouds  $\sim 10$  Myr before the birth of a Pop III main-sequence star (Abel, Bryan & Norman 2002; O’Shea & Norman 2007). This is approximately the end of the initial free-fall phase, the so-called “loitering phase”, where the minimum temperature at this point characterises the fragmentation mass scale (e.g. Omukai & Yoshii 2003). This prescription is similar to the Cen & Ostriker (1992) method but removes the Jeans unstable ( $M_{\text{gas}} > M_J$ ) and cooling timescale ( $t_{\text{cool}} < t_{\text{dyn}}$ ) requirements. We do not consider the former criterion because it is not applicable to simulations that resolve the Jeans length at all times. The molecular hydrogen fraction requirement effectively constrains star formation to cooling molecular clouds, where the  $\text{H}_2$  formation rate is significantly larger than the dissociation rate from a Lyman-Werner radiation field.

If multiple cells meet the star particle formation criteria within 1 pc, we form one Pop III star particle with the centre of mass of these flagged cells to ensure that one massive star is created per metal-free molecular cloud. We randomly sample from an IMF with a functional form of

$$f(\log M)dM = M^{-1.3} \exp \left[ - \left( \frac{M_{\text{char}}}{M} \right)^{1.6} \right] dM \quad (9)$$

to determine the stellar mass. Above  $M_{\text{char}}$ , it behaves as a Salpeter IMF but is exponentially cutoff below that mass (Chabrier 2003). After the star particle forms and its mass is determined, an equal amount of gas is removed from the computational grid in a sphere that contains twice the stellar mass and is centred on the star particle. At this stage of the collapse, a sphere enclosing  $200M_{\odot}$  has a radius of 1–2 pc and has approximately 200 cells. The star particle acquires the mass-weighted velocity of the gas contained in this sphere.

### 3.1.2 Pop II star formation

We treat Pop II star formation with the same prescription as Wise & Cen (2009), which is similar to the Pop III prescription but without the minimum  $\text{H}_2$  fraction requirement. This is removed because the metal-enriched gas can efficiently cool even in the presence of a strong UV radiation field (e.g. Safranek-Shrader, Bromm & Milosavljević 2010). To ensure the volume is cooling, we restrict star formation to gas with temperatures  $T < 1000$  K. Unlike Pop III star particles that represent individual stars, Pop II star particles represent a star cluster of some total mass and an assumed Salpeter IMF.

Once a cell meets these criteria, the prescription searches outward with increasing radius for the boundary of the molecular cloud, centred on the most dense cell. Here,

we define a molecular cloud as a sphere with a dynamical time  $t_{\text{dyn}} = 3$  Myr (corresponding to an average density  $\bar{\rho}_{\text{MC}} \simeq 500\mu \text{ cm}^{-3}$ ) and a radius  $R_{\text{MC}}$ , where  $\mu$  is the mean molecular weight. This sphere typically has a radius of 6 pc (increasing as  $M_{\text{MC}}^{1/3}$ ) for the smallest molecular clouds and 2,500 cells. Once the sphere radius is found, a fraction  $c_{\star} = 0.07f_{\text{cold}}$  of the cold gas ( $T < 10^3$  K) inside the sphere is converted into a star particle with mass  $m_{\star} = c_{\star}(4\pi/3)\bar{\rho}_{\text{MC}}R_{\text{MC}}^3$ . This treatment of cold gas accretion is similar to a star formation model with a multiphase subgrid model (Springel & Hernquist 2003) but is employed in a simulation that can resolve the multi-phase interstellar stellar medium (ISM). After the star particle is created, we replace the sphere with a uniform density  $\rho_{\text{MC}} = (1 - c_{\star})/(Gt_{\text{dyn}}^2)$  and temperature  $T = 10^4$  K, which approximates the initial stages of an H II region.

## 3.2 Stellar feedback

The radiation field is evolved with adaptive ray tracing (Abel & Wandelt 2002; Wise & Abel 2011) that is based on the HEALPix framework (Górski et al. 2005) and is coupled self-consistently to the hydrodynamics. Each star particle is a point source of hydrogen ionising radiation with the ionising luminosity equally split between 48 initial rays (HEALPix level 2). We use a mono-chromatic spectrum for the radiation with the energy  $E_{\text{ph}}$ , the spectral shape weighted photon energy. For a cosmological simulation that focuses on galaxies, this simplification does not significantly affect the overall galactic dynamics (see Sec. 6.3 in Wise & Abel 2011). We do not consider He I and He II ionising radiation. As the rays propagate from the source or into a high resolution AMR grid, they are adaptively split into 4 child rays, increasing the angular resolution of the solution, when the solid angle of the ray  $\theta = 4\pi/(12 \times 4^L)$  is larger than 1/3 of the cell area, where  $L$  is the HEALPix level. We limit the ray splitting to a maximum HEALPix level of 13, or equivalently  $8.05 \times 10^8$  rays per source. We model the  $\text{H}_2$  dissociating radiation with an optically-thin, inverse square profile, centred on all Pop II and III star particles.

### 3.2.1 Population III stellar feedback

We use mass-dependent hydrogen ionising and LW photon luminosities and lifetimes of the Pop III stars from Schaerer (2002). We use a mass-independent photon energy  $E_{\text{ph}} = 29.6$  eV, appropriate for the near-constant  $10^5$  K surface temperatures of Pop III stars. They die as Type II SNe if  $11 \leq M_{\star}/M_{\odot} \leq 40 M_{\odot}$  (Woosley & Weaver 1995; Nomoto et al. 2006) and as PISNe if they are in the mass range 140–260  $M_{\odot}$  (Heger et al. 2003), where  $M_{\star}$  is the stellar mass. For normal Type II SNe between 11–20  $M_{\odot}$ , we use an explosion energy of  $10^{51}$  erg and a linear fit to the metal ejecta mass calculated in Nomoto et al. (2006),

$$M_{\text{Z}}/M_{\odot} = 0.1077 + 0.3383 \times (M_{\star}/M_{\odot} - 11) \quad (10)$$

or equivalently, the metal yield fraction

$$y = 0.3383 - 3.614M_{\star}^{-1}. \quad (11)$$

We model the SNe of stars with  $20 \leq M_{\star}/M_{\odot} \leq 40$  as hypernova with the energies and ejecta masses ( $y \sim 0.15 - 0.2$ )

also taken from Nomoto et al., linearly interpolating their results to  $M_*$ . For PISNe, we use the explosion energy from Heger & Woosley (2002), where we fit the following function to their models,

$$E_{\text{PISN}} = 10^{51} \times [5.0 + 1.304(M_{\text{He}}/M_{\odot} - 64)] \text{ erg}, \quad (12)$$

where  $M_{\text{He}} = (13/24) \times (M_* - 20)M_{\odot}$  is the helium core (and equivalently the metal ejecta) mass and  $M_*$  is the stellar mass. If the stellar mass is outside of these ranges, then an inert, collisionless black hole (BH) particle is created.

The blastwave is modelled by injecting the explosion energy and ejecta mass into a sphere of 10 pc, smoothed at its surface to improve numerical stability (Wise & Abel 2008). Because we resolve the blastwave relatively well with several cells across at its initialization, the thermal energy is converted into kinetic energy and agrees with the Sedov-Taylor solution (e.g. Greif et al. 2007).

### 3.2.2 Population II stellar feedback

Pop II star particles emit 6000 hydrogen ionising photons per stellar baryon averaged over their lifetime and  $E_{\text{ph}} = 21.6$  eV, appropriate for a  $[Z/H] = -1.3$  population (Schaerer 2003). The star particles live for 20 Myr, the maximum lifetime of an OB star. These stars generate the majority of the ionising radiation and SNe feedback in stellar clusters, thus we ignore any feedback from lower mass stars. By considering a constant luminosity, we may be underestimating the impact of radiative feedback because, given an IMF, the total luminosity of a cluster is maximal at early times when thermal and radiation pressure forces are the greatest, i.e. the edge of H II region is still near the massive stars.

For SN feedback, these stars generate  $6.8 \times 10^{48}$  erg  $\text{s}^{-1} M_{\odot}^{-1}$  after living for 4 Myr, which is injected into spheres with a radius of 10 pc. However, if the resolution of the grid is less than 10/3 pc, we distribute the energy into a  $3^3$  cubic region surrounding the star particle. Here, star particles also return ejected material with mass

$$\Delta m_{\text{ej}} = \frac{0.25 \Delta t M_*}{t_0 - 4 \text{ Myr}}, \quad (4 \text{ Myr} < t - t_{\text{birth}} < t_0) \quad (13)$$

back to the grid at every timestep on the finest AMR level.  $t_0 = 20$  Myr denotes the lifetime of the star particle. This ejected gas has solar metallicity  $Z = 0.02$ , resulting in a total metal yield  $y = 0.005$ . However, we note that calculations which are calibrated to Milky Way observations (Madau et al. 1996) suggest  $y \sim 0.02$ , and thus we may be underestimating the Pop II chemical feedback.

## 3.3 Simulation variations

All three simulations start from identical 1 Mpc  $256^3$  initial conditions, have the same refinement criteria, and use the same star formation and feedback models. Starting with our reference model in Paper I, each following simulation builds upon the physics of the previously described one.

### 3.3.1 Reference model

We use the nine-species (H I, H II, He I, He II, He III,  $e^-$ ,  $\text{H}_2$ ,  $\text{H}_2^+$ ,  $\text{H}^-$ ) non-equilibrium chemistry model

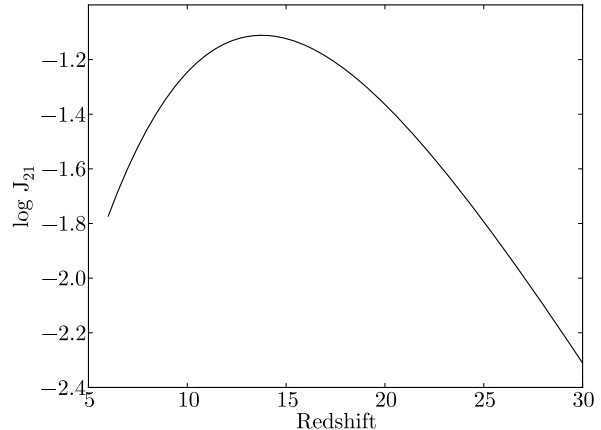


**Figure 2.** Time evolution of the Lyman-Werner background in units of  $J_{21} = 10^{-21}$  erg  $\text{s}^{-1} \text{cm}^{-2} \text{Hz}^{-1} \text{sr}^{-1}$ , calculated with the Wise & Abel (2005) model. See eq. (16) for its functional fit.

in ENZO (Abel et al. 1997; Anninos et al. 1997) and the  $\text{H}_2$  cooling rates from Glover & Abel (2008). We spatially distinguish metal enrichment from Pop II and Pop III stars, however they do not contribute to the radiative cooling rates and act as passive tracer fields for the SNe ejecta. We will refer to this simulation as the “Base” simulation. It required 150,000 CPU hours on 512 compute cores to run to  $z = 8.1$ .

### 3.3.2 Metal cooling

In this simulation, we only add the effects of radiative cooling from fine-structure transitions in metals. We will refer to this simulation as the “MC” simulation. We use the method of Smith, Sigurdsson & Abel (2008) that is incorporated into ENZO v2.0. We calculate the cooling rates with CLOUDY 07.02.01, which has a sophisticated chemical network that includes all atomic species and many molecular species<sup>2</sup>, on a logarithmically spaced 4-dimensional grid of (i) density –  $10^{-6}$  to  $10^6 \text{ cm}^{-3}$ ,  $\Delta = 0.25$  dex, (ii) temperature – 10 to  $10^8$  K,  $\Delta = 0.1$  dex, (iii) electron fraction –  $10^{-6}$  to 1,  $\Delta = 0.25$  dex, and (iv) metallicity –  $10^{-6}$  to 1  $Z_{\odot}$ ,  $\Delta = 1$  dex, where  $\Delta$  is the spacing between grid points. We use the CMB radiation spectrum as the input spectrum. Dust cooling becomes important at  $\gtrsim 10^9 \text{ cm}^{-3}$ , which our simulations are not designed to probe, and thus we do not consider cooling from dust grains. It required 200,000 CPU hours on 512 compute cores to complete. Compared to the Base simulation, the additional compute time comes from ray tracing through a larger ionised volume, i.e. the rays are not terminated when fully absorbed.

### 3.3.3 Radiation pressure and soft UV background

This simulation adds momentum transfer from ionising radiation to gas and an  $\text{H}_2$ -dissociating radiation back-

<sup>2</sup> Because the cooling rates from rotational and vibrational  $\text{H}_2$  transitions are already included in ENZO, thus we do not include  $\text{H}_2$  cooling in the CLOUDY rate table.

ground. We will refer to this simulation as the ‘‘RP’’ simulation, and the runtime is similar to the Base simulation at 150,000 CPU hours. As the radiation field is calculated with ENZO+MORAY, the momentum of absorbed ionising radiation

$$d\mathbf{p}_{\text{rp}} = \frac{dP E_{\text{ph}}}{c} \hat{\mathbf{r}} \quad (14)$$

is transferred to the absorbing medium, where  $dP$  is the number of photons absorbed,  $E_{\text{ph}}$  is the photon energy, and  $\hat{\mathbf{r}}$  is the normal direction of the radiation. This additional momentum further accelerates the gas by

$$d\mathbf{a}_{\text{ap}} = \frac{d\mathbf{p}_{\text{rp}}}{dt \rho V_{\text{cell}}} \quad (15)$$

per unit mass, where  $\rho$  is the gas density,  $dt$  is the radiative transfer timestep, and  $V_{\text{cell}}$  is the cell volume. Currently we do not consider momentum transfer by radiation trapping when UV light is absorbed by dust grains and re-emitted in the IR and absorbed many times. In principle, this would increase the  $d\mathbf{a}_{\text{ap}}$  by a factor of  $f_{\text{trap}}$ , which we discuss in Section 5.2. The acceleration  $d\mathbf{a}_{\text{ap}}$  is then added to the acceleration field in the calculation, for example, from gravity, in an operator split fashion.

A time-dependent Lyman-Werner (LW) optically thin radiation background is utilised in this simulation on which the LW radiation from point sources are added. LW flux from point sources dominates over the background within 3 kpc, dissociating  $\text{H}_2$  and thus delaying Pop III star formation in nearby haloes (Machacek, Bryan & Abel 2001; Wise & Abel 2007b; O’Shea & Norman 2008). To calculate its intensity as a function of time, we use the semi-analytical model of Wise & Abel (2005), updated with the 7-year WMAP parameters and optical depth to Thomson scattering. The LW radiation intensity is plotted in Fig. 2. In this semi-analytical model, we use a Pop III stellar mass of  $100 M_{\odot}$ , star formation efficiency of 0.005, and escape fraction of 0.2 (Wise & Cen 2009). The intensity decreases after  $z \sim 14$  because Pop II star formation becomes dominant, which produce less LW specific luminosity than Pop III stars that have surface temperatures of  $T = 10^5$  K. For computational convenience, we fit the background evolution with the function

$$\log_{10} J_{21}(z) = A + Bz + Cz^2 + Dz^3 + Ez^4, \quad (16)$$

where  $(A, B, C, D, E) = (-2.356, 0.4562, -0.02680, 5.882 \times 10^{-4}, -5.056 \times 10^{-6})$  and  $J_{21}$  is the specific intensity in units of  $10^{-21} \text{ erg s}^{-1} \text{ cm}^{-2} \text{ Hz}^{-1} \text{ sr}^{-1}$ . This fits the model data within 1 per cent in  $6 \leq z \leq 30$  and is consistent with  $J_{21}$  values in Trenti & Stiavelli (2009).

## 4 RESULTS

We concentrate on the most massive halo in the simulation to demonstrate the effects of momentum transfer from ionising radiation. For reasons discussed later, the halo in the MC simulation overcools and forms stars at high specific SFR, which ionises the entire simulation volume at  $z = 8.1$ . Solving the radiative transfer equation with ENZO+MORAY in this simulation becomes computationally unfeasible in the optically thin limit, so we stop the MC simulation here and compare the halo in the three simulations that this point.

At redshift 8.1, the halo has a DM mass of  $2.0 \times 10^8 M_{\odot}$ , corresponding to a virial temperature  $1.7 \times 10^4$  K and circular velocity of  $21 \text{ km s}^{-1}$ . This halo experienced a major merger at  $z \sim 10$ . It is undergoing a major merger at  $z = 8.1$  that increases the virial temperature to  $> 10^4$  K at which point it can efficiently form stars. The gas fraction of the halo  $f_g = M_{\text{gas}}/M_{\text{tot}}$  has recovered to 0.13, previously being depleted to under 5 per cent in the Pop III hosting progenitors that had its gas expelled by stellar and supernova feedback. Here  $M_{\text{tot}}$  is the total mass (including DM) of the halo. At this time, the Base, MC, and RP simulations have a stellar mass of  $2.5 \times 10^5$ ,  $6.7 \times 10^5$ , and  $4.5 \times 10^5 M_{\odot}$ , respectively. By redshift 7, its total mass is  $1.0 \times 10^9 M_{\odot}$ , containing  $2.1 \times 10^6 M_{\odot}$  of stars in the Base simulation. We refer the reader to Paper I for more details at  $z = 7$ .

### 4.1 Comparison of star formation histories

The top panel in Figure 3 shows the evolution of the ionised volume fraction of all three simulations. The second, third, and fourth panels show the star formation rate (SFR). The specific SFR (sSFR), the gas accretion rate  $\dot{M}_{\text{gas}}$ , and the ratio of SFR to  $\dot{M}_{\text{gas}}$  are shown in the bottom three panels. At redshift 12, both MC and RP simulations produce metal-enriched stars after the halo reaches the filtering mass (Gnedin & Hui 1998; Gnedin 2000; Wise & Abel 2008) of  $\sim 10^7 M_{\odot}$ . The burst in the Base simulation is slightly delayed and weaker by an order of magnitude because of the lack of metal cooling. In all three simulations, about 15 per cent of the accreted gas is converted into stars. Radiative and supernova feedback in the stronger bursts of the MC and RP runs drive a net outflow from the halo, seen in negative values of  $\dot{M}_{\text{gas}}$ .

The halo continues to accrete from numerous minor mergers of  $\sim 10^6 M_{\odot}$  haloes until  $z = 8.1$ . One notable difference in the RP simulation is the enhanced gas accretion between redshift 9 and 10. Here, the UV background suppresses Pop III star formation in minihaloes by increasing the minimum mass to cool and condense by  $\text{H}_2$  alone (Machacek, Bryan & Abel 2001; Wise & Abel 2007b; O’Shea & Norman 2008). This results in more gas-rich mergers, thus increasing the gas accretion rate. The halo continues this constant but slow mass buildup until a major merger at  $z = 8.1$ . Before the major merger, the SFRs are similar between  $10^{-2}$  and  $10^{-3} M_{\odot} \text{ yr}^{-1}$  in the simulations with the RP simulation sustaining a more consistent SFR mainly because of the additional gas accretion whereas the other simulations have more a bursty behavior. The galaxies convert between 0.1 and 1 per cent of the accreted gas into stars during this quiescent period before it reaches a virial temperature of  $10^4$  K.

The most significant difference between the simulations is the star formation when the halo reaches a virial temperature of  $10^4$  K through a major merger. The Base simulation has a SFR =  $3.7 \times 10^{-3} M_{\odot} \text{ yr}^{-1}$  and a sSFR =  $15 \text{ Gyr}^{-1}$ . In the MC simulation, the additional radiative cooling provided by the metal lines prompts a SFR =  $9.9 \times 10^{-2} M_{\odot} \text{ yr}^{-1}$  and a sSFR =  $150 \text{ Gyr}^{-1}$ , an order of magnitude higher than the Base simulation. The radiative and supernovae feedback from these stars drives a net gas outflow of  $-0.2 M_{\odot} \text{ yr}^{-1}$  from the halo, as seen in the fourth panel of Figure 3, but cannot abate the star formation alone. Momen-

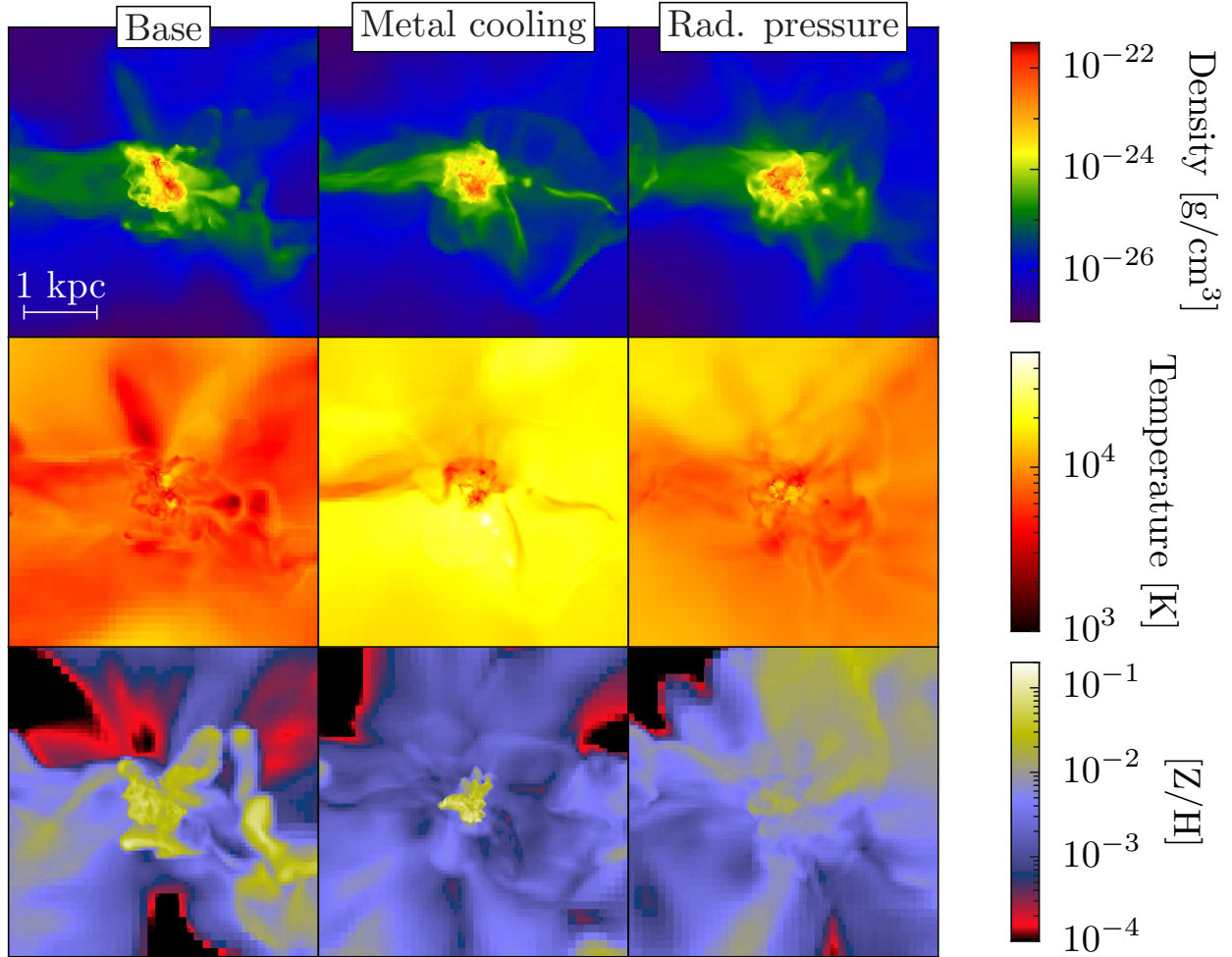


**Figure 4.** A visual comparison of the most massive ( $2.3 \times 10^8 M_\odot$ ) halo at  $z = 8.1$  in simulations with the base physics model (left column), including radiative cooling from metal species (middle column), and including radiation pressure and an  $H_2$ -dissociating background (right column). The different rows contain density-weighted projections of gas density (top), temperature (middle), and total metallicity (bottom). The field of view is two virial radii (3.4 kpc). Comparing the Base and Metal Cooling simulations, the metal-rich ejecta cannot expand before all of its thermal energy is radiated away, primarily through the additional metal cooling. The additional impetus from radiation pressure alleviates this artifact and can regulate star formation by driving gas outflows and further entrainment with the surrounding medium.

tum input from massive stars in the RP simulation reduces the SFR by a factor of five to  $1.8 \times 10^{-2} M_\odot \text{ yr}^{-1}$  and the sSFR to  $37 \text{ Gyr}^{-1}$ . On average, approximately 3 per cent of the accreted gas forms stars in the latest star formation period, and the variations are caused by stellar feedback. At  $z = 8.1$ , the enhanced star formation in the MC simulation ionises 96 percent of the simulation volume, which is in stark comparison with the Base and RP simulations with ionised fractions of 42 and 36 percent, respectively. The RP ionised fraction is slightly lower because of the suppression of Pop III SF from the LW background.

Observations of star-forming galaxies show a tight relation between sSFR and stellar mass, and we can compare our results to determine our most physical model. Massive ( $M_* \geq 10^{10} M_\odot$ ) galaxies at  $z \geq 2$  have  $\text{sSFR} \propto M_*^{-0.4}$ , flattening to an upper threshold of  $2.5 \text{ Gyr}^{-1}$  in low-mass galaxies (Karim et al. 2011). At  $z = 4 - 6$ , Stark et al. (2009) found a strong  $\text{sSFR}-M_*$  correlation with a simi-

larly large scatter (see Figure 1 in Khochfar & Silk 2011). In that work, the average SFR is  $\sim 3 M_\odot \text{ yr}^{-1}$  in systems between  $M_* = 10^8$  and  $10^{11} M_\odot$ , or equivalently, an average of  $30 \text{ Gyr}^{-1}$  in stellar systems of  $10^8 M_\odot$ . Galaxies at  $z \gtrsim 7$  also show a large scatter in sSFR, ranging from 1 to  $100 \text{ Gyr}^{-1}$  for galaxies with stellar masses between  $10^7$  and  $10^9 M_\odot$ , trending toward higher sSFRs in smaller systems (Schaerer & de Barros 2010; McLure et al. 2011; Khochfar & Silk 2011). Do high-redshift galaxies have more gas available for star formation to sustain  $\text{sSFR} > 2.5 \text{ Gyr}^{-1}$ , as suggested by the  $z \gtrsim 7$  data? Does this relation continue to the very smallest galaxies at high-redshift? If we assume so, the MC simulation produces the best match with the other models falling below the relation. This goes against intuition in that a more realistic model, in our case, adding radiation pressure and a LW background, produces more realistic galaxies. To further understand this behav-



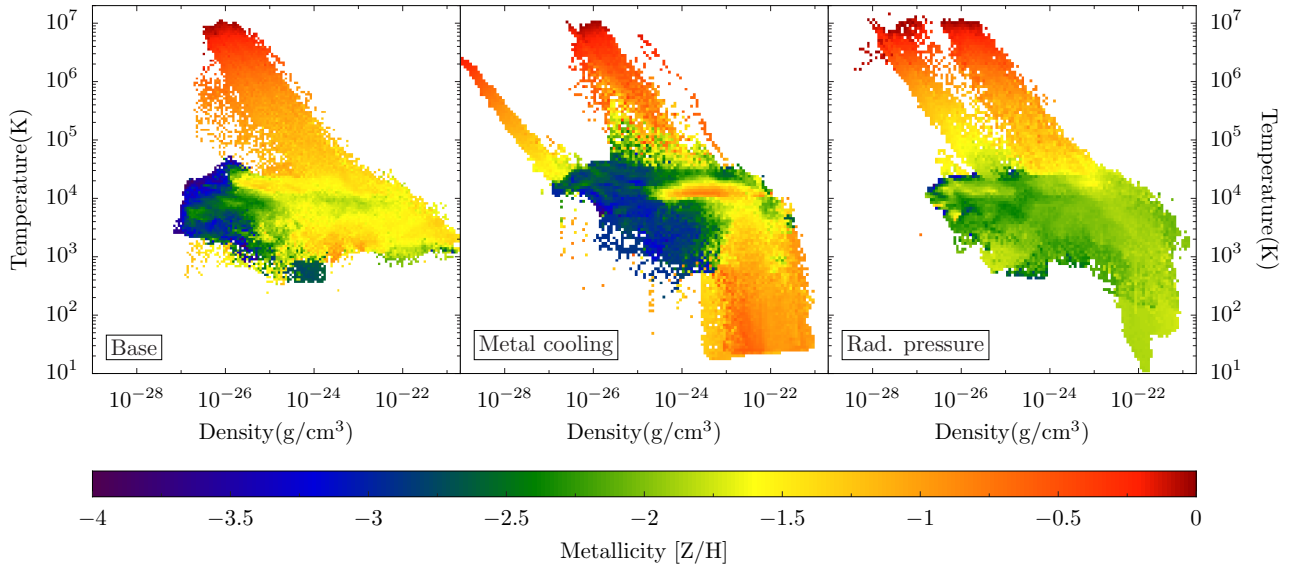


**Figure 5.** Mass-weighted average metallicities as a function of density and temperature in the most massive halo at  $z = 8.1$  for the Base (left), metal cooling (middle), and radiation pressure (right) simulations. When metal cooling is considered, metal-rich gas above  $3 \times 10^{-23} \text{ g cm}^{-3}$  can cool to the CMB temperature. The majority of gas with  $> 10^{-2} Z_{\odot}$  is restricted to SN remnants (hot ISM phase up to  $T = 10^7 \text{ K}$ ) and cold and dense gas. The metals are not mixed into the lower density ISM. Radiation pressure (right panel) provides an additional impetus to mix the metal-rich ejecta with the entire ISM, resulting in nearly all of phase-space being enriched to an average of  $\sim 10^{-2} Z_{\odot}$ .

ior, we must investigate the gaseous properties and stellar population of the galaxy.

#### 4.2 Overcooling and artificially enhanced star formation

Here we concentrate on the causes behind the enhanced star formation in the metal cooling simulation when compared to the Base simulation. Figure 4 shows density-weighted projections of gas density, temperature, and total metallicity for the three simulations. The gas distributions are irregular and have no organised disc rotation in any of the runs. There are three DM filaments that accrete onto the halo, which is typical of rare peaks (e.g., Dekel et al. 2009; Danovich et al. 2011). Only one filament has retained its gas, which is located to the left of the halo in Figure 4. The other filaments have been photo-evaporated and Jeans-smoothed by stellar radiation. As previously mentioned, the MC simulation is nearly fully ionised with an average intergalactic medium (IGM) temperature of  $\sim 3 \times 10^4 \text{ K}$ , clearly seen in the temperature projections. The additional pressure provided by the heated IGM compresses the filament in comparison with the Base and RP simulations.

The spatial metallicity distributions are the most relevant in understanding the SFR deviations between the simulations. In the Base simulation, the metal-rich outflows with  $[Z/H]$  between  $-1$  and  $-2$  can be seen expanding out to a radius of  $\sim 1 \text{ kpc}$ . The MC simulation produces a factor of three more stars, but the metal-rich ejecta are restricted in a small volume with a radius of  $\sim 0.5 \text{ kpc}$  with a mean metallicity of  $[Z/H] = -0.5$ . These metal-rich regions are surrounded by a metal-poor interstellar medium (ISM) with  $-4 < [Z/H] < -2$ .

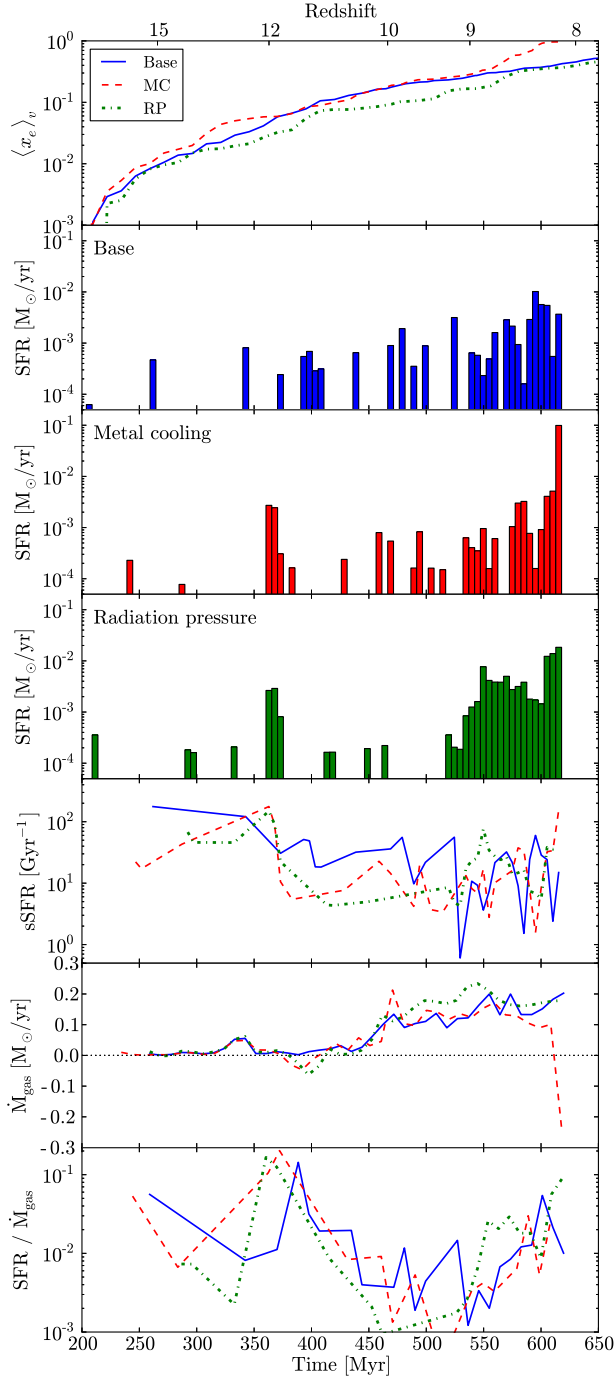
Figure 5 shows the metallicity as a function of density

and temperature, and it further illustrates the differences that metal cooling induces. Without metal cooling in the Base simulation, the gas can only cool to  $\sim 1000 \text{ K}$  through  $\text{H}_2$  cooling in the gas phase. The metals are mixed to an average of  $3 \times 10^{-2} Z_{\odot}$  in gas with  $\rho > 3 \times 10^{-26} \text{ cm}^{-3}$ . The nearly solar metallicity isobars reaching  $10^7 \text{ K}$  are Type II SNe remnants. When metal cooling is considered, the relatively metal-rich ( $10^{-1} Z_{\odot}$ ) material is mainly confined to the cold phase of the ISM above  $1 \text{ cm}^{-3}$  and below  $1000 \text{ K}$  down to the CMB temperature. This cold, metal-rich gas mixes little with the surrounding diffuse ISM that has a mean metallicity of  $10^{-3} Z_{\odot}$ .

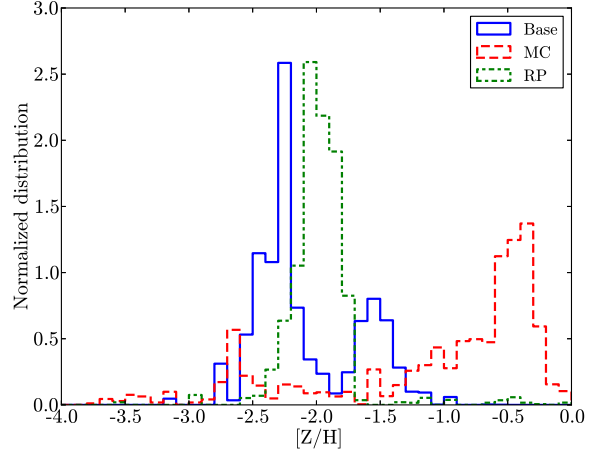
Because stars form in cold and dense gas, the stellar metallicities reflect the gas metallicities in the cold phase. They can be a plausibility check as they can be indirectly compared to observed metallicities in local dwarf galaxies, which have a clear luminosity-metallicity relationship that increases from  $[\text{Fe}/\text{H}] = -2.5$  to  $-1.5$  over a luminosity range  $\log(L/L_{\odot}) = 3-7$  (Kirby et al. 2011).

Figure 6 compares the metallicity distribution functions (MDFs) in the most massive galaxy at  $z = 8.1$  in each simulation. The Base simulation has a bimodal distribution within the range  $-2.5 < [Z/H] < -1.0$ . The lower metallicity stars were formed before the halo reaches  $T_{\text{vir}} = 10^4 \text{ K}$ . Afterward, the stars quickly enrich the halo to  $[Z/H] \sim -1.5$ , which forms stars at similar metallicities, creating a bimodal MDF. This process is described in more detail in Paper I. A similar enhancement in star formation occurs in the MC simulation at  $T_{\text{vir}} = 10^4 \text{ K}$  but to a greater extent because of higher cooling rates and thus star formation rates. Stars primarily form in the inner  $500 \text{ pc}$ , where the gas is enriched to  $[Z/H] \sim -0.5$  because the metal-rich ejecta is confined within these inner regions.

These metallicities are a factor of 30 above the



**Figure 3.** The top panel shows the ionised volume fraction, while the next three panels show the star formation history for the reference, metal cooling, and radiation pressure simulations. The fifth panel displays the specific star formation rate for all three simulations. The sixth panel shows the gas accretion rate in the halo, and the bottom panel shows the ratio of star formation and gas accretion, which is effectively the star formation efficiency. Including metal cooling results in overcooling in the halo interior, efficiently producing stars at a rate of  $\sim 0.1 M_\odot \text{ yr}^{-1}$ . This single burst ionises the entire simulation box. Radiation pressure from ionising radiation regulates star formation to  $\sim 0.01 M_\odot \text{ yr}^{-1}$ .



**Figure 6.** Normalised stellar metallicity distribution functions of the most massive halo for the Base (solid lines), metal cooling (dashed), and radiation pressure (dash-dotted) simulations at  $z = 8.1$ . Overcooling in the metal cooling simulation creates a stellar population that is nearly solar metallicity, whereas the additional mixing with radiation pressure shifts the average back to  $\sim 10^{-2} Z_\odot$ , agreeing with the mass-metallicity relation of galaxies.

luminosity-metallicity relationship and suggest that our MC model produces galaxies that are too luminous and metal-rich. The extra radiative cooling from metal species allows for the super-solar SNe ejecta to lose most of its thermal energy before it launches a high-velocity outflow, and most of the ejecta are trapped within the galaxy. Then this metal-rich material cools again and condenses into star forming clouds. This process repeats several times, creating a runaway effect in overproducing stars, known as the well-known and studied numerical “overcooling problem” that produces galaxies that are too centrally concentrated (first reported by Katz, Weinberg & Hernquist 1996). This was solved by introducing SNe feedback and conducting the simulations at higher resolutions; however, our calculations show the same problem at parsec-scale spatial resolution and despite resolved SNe feedback.

### 4.3 Effects of radiation pressure

We find that momentum transfer from ionising radiation to the absorbing gas alleviates the overcooling problem seen in the MC simulation. Recall that at  $z = 8.1$ , the SFR is reduced by a factor of five compared to the MC simulation. To understand this difference, we focus on its effect on internal gas dynamics and the chemo-thermal state of the gas, the increased ejecta dispersion from their origin, and the ensuing star formation.

#### 4.3.1 Gas dynamics

Unlike the thermal energy produced by SN feedback, momentum must be conserved and is not lost to radiative processes. The momentum transferred to the absorbing gas generates a medium in the central 100 pc that is both turbulent and expanding radially, where the young stars and

their H II regions are clustered. As the D-type shocks expand with the ionisation fronts, momenta from the absorbed photons are transferred to the optically thick shock. Their cumulative action produces an average outflow in the inner 100 pc, which is visible in the radial profile of the mass-averaged radial velocity, shown in the top panel of Figure 7. The radial velocity is calculated after subtracting the mass-averaged bulk velocity of the halo. In the central 15 pc, the mass-averaged radial velocity is  $20 \text{ km s}^{-1}$ , and it gradually decreases to  $2 \text{ km s}^{-1}$  at 40 pc. This weak expansion of the inner dense gas extends out to 100 pc. In contrast, the Base and MC simulations both exhibit weak inflows up to  $5 \text{ km s}^{-1}$ , where SN feedback is not enough to support the dense central gas.

Within the inner 100 pc, there are 49 young ( $< 20 \text{ Myr}$ ) star particles with a total mass of  $4.6 \times 10^4 M_{\odot}$ . The interaction between the expanding shocks associated with their H II regions and SN blastwaves creates and sustains this turbulent medium. To measure the turbulent motions, we calculate the three-dimensional rms velocity  $v_{\text{rms}}$  as a function of radius. It is computed with respect to the mass-averaged velocity of each thick shell. On average, it is  $\sim 20 \text{ km s}^{-1}$  and varies little with radius, indicating that turbulence is widespread throughout the halo. The turbulence is mildly supersonic at  $r > 100 \text{ pc}$  with turbulent Mach numbers  $M_{\text{turb}} = \langle v_{\text{rms}} \rangle / \langle c_s \rangle$  decreasing with radius from two at the virial radius, where  $c_s$  is the sound speed and the angled brackets denote a mass-weighted average in the shell. This is nearly the circular velocity of the halo,  $V_c = 21 \text{ km s}^{-1}$ . In the inner 50 pc,  $v_{\text{rms}} \sim 20 \text{ km s}^{-1}$ , and it slowly decreases to  $15 \text{ km s}^{-1}$  at 130 pc and increases to  $20 \text{ km s}^{-1}$  at the virial radius. Outside 300 pc, radiation pressure has little effect on turbulent motions, where it is primarily driven by virialization (Wise & Abel 2007a; Greif et al. 2008). The Base simulation drops to  $10 \text{ km s}^{-1}$  within  $r = 100 \text{ pc}$  as the gas cools and condenses. The loss of gaseous kinetic energy is even more apparent with metal cooling, lowering  $v_{\text{rms}}$  to  $5 \text{ km s}^{-1}$  in the inner 50 pc. This is consistent with an over-cooling core that is not pressure supported by either thermal or turbulent energy.

Interestingly, the turbulent Mach numbers, shown in the bottom panel of Figure 7, are almost identical in the MC and RP models in the inner 100 pc. This occurs even though the addition of momentum feedback creates a  $v_{\text{rms}}$  four times larger than the MC simulation. This behavior is caused two complimentary processes. First, radiation pressure creates a more diffuse medium in which the SN explosions occur, which results in a lower cooling rate and keeps the temperatures and, equivalently, sound speeds high. Second, the additional driving from radiation pressure and blastwaves that have not stalled in the ISM keep the turbulent velocities nearly equal to the halo circular velocity. These physical processes lead to an unchanged turbulent Mach in both star forming environments.

The velocity dispersion is a good measure of the general strength of turbulent motions, but the vorticity  $\omega$  better characterises the local strength of turbulence. In Figure 8, we plot two-dimensional histograms of vorticity (top panels) as a function of radius and its growth (bottom panels), which is the right hand side of Equation (8). For the RP simulation, we include the baroclinic term from radiation pressure in our analysis,  $(\mathbf{a}_{\text{rp}} \times \nabla \rho) / \rho$ . To visualise the fluid flow, it is

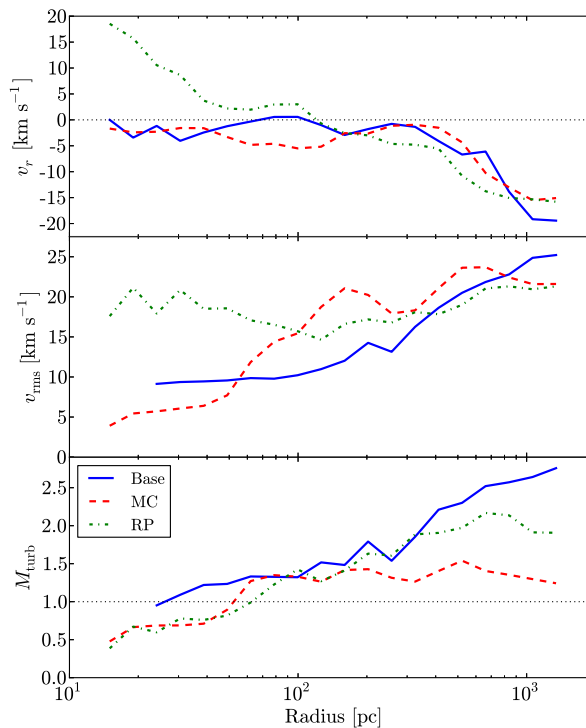


**Figure 7.** *Top panel:* Mass-weighted radial profiles of gas radial velocity of the most massive halo, centred on the halo’s centre of mass, from the reference (solid), metal cooling (dashed), and radiation pressure (dash-dotted) simulations. The Base and MC runs exhibit a zero to small inflow velocity within 300 pc, whereas adding radiation pressure results in an average gas outflow in the inner 100 pc. *Middle panel:* Three-dimensional rms velocity as a function of radius, illustrating the turbulent medium created by momentum transfer from ionising radiation. Turbulent motions support the object from further collapsing and assist to mix the metal-rich ejecta with the metal-poor ISM. *Bottom panel:* Radial profile of the turbulent Mach number  $M_{\text{turb}}$ . The MC and RP simulations exhibit nearly identical  $M_{\text{turb}}$  values in the inner 100 pc, showing that the turbulence decays in the MC run as the gas rapidly cools.

helpful to consider the local rotational period is  $4\pi/|\omega|$ . Gas with the highest vorticities exist at  $100 \lesssim r/\text{pc} \lesssim 500$ . This is primarily driven by virial shocks as matter is accreted from the IGM and filaments. This region is approximately where the density increases by an order of magnitude in the density projections of Figure 4. The MC and RP simulations have similar average vorticities until  $r \lesssim 50 \text{ pc}$ , where the RP simulation exhibits an increase of 10, whereas the MC simulation stabilises at  $2 \times 10^{-14} \text{ s}^{-1}$ . Vorticity generation is significantly higher by a factor of 100 within this inner region with radiation pressure. We find that non-barotropic flows from thermal pressure are primarily responsible for sustaining these turbulent motions. The contribution from vorticity stretching and radiation pressure provides  $\sim 10^{-1}$  and  $\sim 10^{-5}$  of  $D\omega/Dt$ , respectively. The very weak driving from radiation pressure does not necessarily indicate that it can be neglected. Because it adds momentum to the shells, the shocks during shell collisions are stronger and produce more

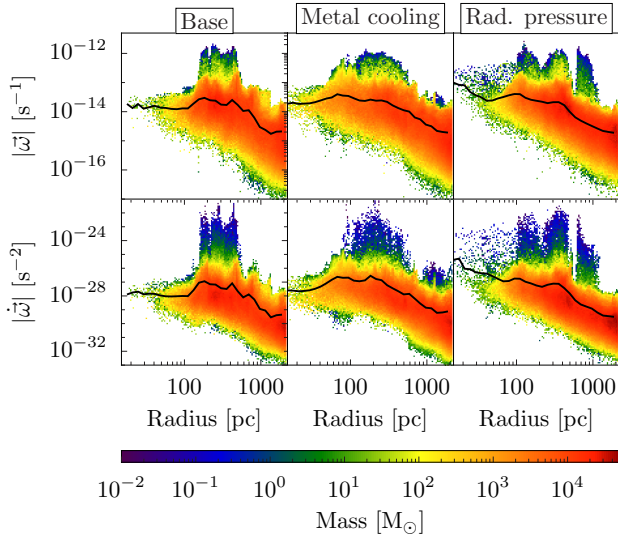


**Figure 8.** *Top row:* Mass-weighted histograms of the magnitude of vorticity for the Base, MC, and RP runs from left to right. The mass-weighted radial profile of vorticity is shown by the solid line. *Bottom row:* Total time derivative of vorticity, i.e. right hand side of Equation (8). Within the inner  $\sim 70$  pc, vorticity is generated at a higher rate in the RP simulations than the Base and MC cases, leading to a more turbulent medium that is also depicted in the rms velocity (Figure 7).

vorticity through the thermal baroclinic term. The weak contribution from radiation pressure is straightforward to understand. It is strongest when the ionisation front radius is small, and the H II is close to spherical. In the spherically symmetric case, radiation will always be absorbed parallel to the density gradient as the optical depth increases, and thus  $\mathbf{a}_{\text{rp}} \times \nabla \rho$  is small. In a clumpy medium, this term will be larger when radiation grazes the surface of dense clumps. It should be noted that by neglecting scattering we could be underestimating its magnitude, and our calculations are conservative in quantifying the impact of radiation pressure in the ISM of dwarf galaxies.

#### 4.3.2 Metal mixing

The gas metallicity shown in Figure 4 show that the SN ejecta has expanded beyond the virial radius with outflows with velocities up to  $250 \text{ km s}^{-1}$ , enriching most of the gas to  $[Z/H] \sim -2$ . This behaviour is further illustrated in Figure 5, where the SN ejecta thoroughly mixes with the ISM at all density-temperature pairs in the cold and warm phases. This greatly differs from the lack of mixing in the MC simulation that creates a distinct separation between dense metal-rich gas and diffuse metal-poor gas.

Metal mixing is enhanced by a sustained turbulent medium, resulting in a MDF (Fig. 6) with a mean metallicity of  $[Z/H] = -2.1$  and a standard deviation of 0.2 dex. This is in excellent agreement with the luminosity-metallicity relationship for dwarf galaxies for a stellar system of  $M_{\star} = 4.5 \times 10^5 M_{\odot}$  (Kirby et al. 2011). This agreement suggests that radiation pressure plays an important role in regulating star formation in high-redshift dwarf galaxies.

#### 4.3.3 Star formation regulation

We have demonstrated that momentum input from massive stars prevents the overcooling and over-enrichment of the gas in galaxy formation simulations. The additional momentum from radiation both disperses the metal-rich SN ejecta to large radii and provides turbulent support to the system. The first effect reduces the metallicity in the dense gas. This reduces the radiative cooling from metal species and the amount of cold, dense gas available for star formation. The latter effect prevents the gaseous core from catastrophically collapsing and forming stars at a high efficiency.

Our comparison between the MC and RP simulations shows that star formation is self-regulated with radiation pressure playing a vital role in early galaxy formation. To reiterate, the RP simulation creates a galaxy with a sSFR =  $37 \text{ Gyr}^{-1}$  and a stellar population whose MDF ( $\langle Z/Z_{\odot} \rangle = -2.1$ ) is in excellent agreement with observations of local dwarf galaxies.

#### 4.4 Radiation pressure characteristics

Here we describe some of the properties of radiation pressure within our largest galaxy. Figure 9 shows two-dimensional slices of acceleration from momentum transfer  $a_{\text{rp}}$  (Equation 15), gas density, temperature, and total metallicity through the centre of mass of the galaxy. The acceleration  $a_{\text{rp}}$  is scaled with respect to the gravitational acceleration at the virial radius,  $a_{\text{grav}} = GM_{\text{vir}}/r_{\text{vir}}^2 = 7.0 \times 10^{-10} \text{ cm s}^{-2}$ . The time to accelerate the gas above the escape velocity  $v_{\text{esc}} = (2GM_{\text{vir}}/r_{\text{vir}})^{1/2}$  is

$$t_{\text{esc}} = v_{\text{esc}}/a_{\text{grav}} = [50\Omega_m(z)H^2(z)]^{-1/2} \quad (17)$$

which is independent of the halo. Here  $\Omega_m(z)$  and  $H(z)$  are the matter density and Hubble constant at redshift  $z$ . In a matter dominated universe ( $z \gg 1$ ) for the adopted  $\Lambda$ CDM cosmology, this timescale is  $120[(1+z)/10]^{-3/2} \text{ Myr}$ , which is possible with sustained star formation in a galaxy. However, this should be only be used to gauge the instantaneous impact of the momentum transfer because the acceleration will decrease as the shell travels farther from the source.

The density plot shows that the ISM is fractal and porous in nature with the H II regions, creating dense shells on their surfaces. The acceleration  $a_{\text{rp}}$  exceeds 10 per cent of  $a_{\text{grav}}$  in most of the H II region except for the interiors of the SN remnants, where the neutral hydrogen fraction is nearly zero. It exceeds  $a_{\text{grav}}$  in the dense, neutral shells surrounding the H II regions. Figure 10 shows the probability and cumulative distribution function of  $a_{\text{rp}}/a_{\text{grav}}$  inside of this halo. There is a plateau in the distribution between  $2 \times 10^{-3}$  and 0.3 at  $2 \times 10^6 M_{\odot}$  per dex. Radiation pressure is accelerating about 4 per cent ( $\sim 3 \times 10^5 M_{\odot}$ ) of the halo gas greater than  $a_{\text{grav}}$ .

The slices of temperature and total metallicity in Figure 9 show the hot phase of the ISM, which have  $T > 10^6 \text{ K}$  and approximately solar metallicity. Our stellar feedback prescription injects SN thermal energy and metals after 4 Myr of main sequence radiative feedback. Consequently, the SN remnants are initially contained within the rarefied medium of the interior of their associated H II regions and then ex-

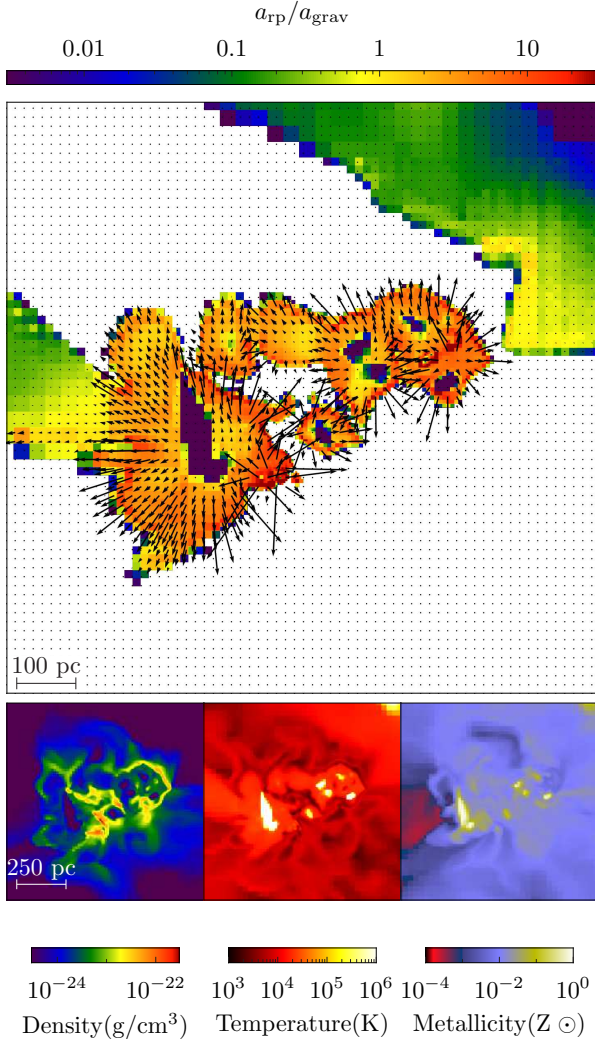


**Figure 9.** Top panel: Slices of instantaneous acceleration from momentum transfer from absorbed ionising radiation, which has been scaled to the total gravitational acceleration of the halo,  $a_{\text{grav}} = GM_{\text{vir}}/r_{\text{vir}}^2$ . Larger values indicate a greater outward acceleration from the responsible star particle. The arrows denote the direction and magnitude of the acceleration field. The field of view is 1 kpc and is cut through the halo’s centre of mass. Bottom panels: The same field of view for gas density (left), temperature (middle), and metallicity (right).

pand into the ISM, and in some cases, they drive metal-rich outflows into the IGM.

## 5 DISCUSSION

Stellar feedback comes in various forms. First, photo-ionisation and photo-heating from massive stars create H II regions that provide pressure support to the warm phase of the ISM. An extreme case of photo-heating feedback exists in haloes with  $M \lesssim 10^7 M_{\odot}$  that host Pop III stars, where the  $\sim 30 \text{ km s}^{-1}$  shock launched by the H II region can expel over 90 per cent of the gas from the halo (Whalen, Abel & Norman 2004; Kitayama et al. 2004; Abel, Wise & Bryan 2007). Second, SNe feedback injects thermal energy and heavy elements into the ISM, creat-

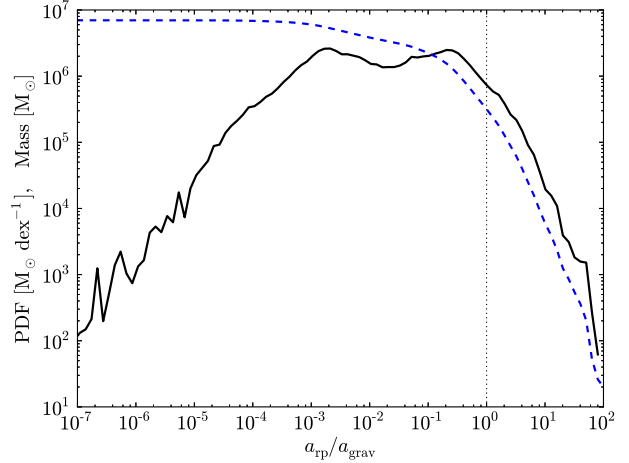


**Figure 10.** Mass-weighted probability density distribution (solid line) of the instantaneous acceleration from momentum transfer from absorbed ionised radiation, which has been scaled to  $a_{\text{grav}} = GM_{\text{vir}}/r_{\text{vir}}^2 = 7.0 \times 10^{-10} \text{ cm s}^{-2}$ , inside the virial radius of the most massive galaxy. The inverse cumulative distribution is shown by the dashed line. Four per cent ( $\sim 3 \times 10^5 M_{\odot}$ ) of the gas is experiencing an acceleration greater than the total gravitational force of the halo.

ing the hot bubbles and blastwaves. They can self-enrich their environment (e.g. Wise et al. 2012), disrupt its star-forming cloud (e.g. Draine & Woods 1991; Whalen et al. 2008), create realistic bulgeless disc galaxies, and possibly launch large-scale outflows (Governato et al. 2010; Brook et al. 2012). Both processes together can play an important role in regulating star formation and altering gas and stellar metallicities, galactic morphologies, gas fractions, and the structure of the ISM.

Another feedback process is the momentum transfer from ionising radiation from massive stars, i.e. radiation pressure. It has been suggested that radiation pressure can regulate star formation and launch galactic outflows in large galaxies (Haehnelt 1995; Murray, Quataert & Thompson 2005; Murray, Ménard & Thompson 2011; Hopkins, Quataert & Murray 2011). In this paper, we have investigated the role of momentum deposition from ionising radiation in the formation of high-redshift dwarf galaxies. We have found that the addition of radiation pressure regulates star formation through additional turbulent support from shell collisions and allowing for SNe to drive large-scale outflows from the galaxy, ejecting metal-rich gas in the process. These effects alleviate the galaxy overcooling problem seen in various simulations of galaxy formation.

By including radiation pressure, our simulation creates realistic high-redshift dwarf galaxies that matches the local luminosity-metallicity relation. Although this is not a direct comparison between high-redshift and local dwarf galaxies, the metallicities of the stellar population is a good gauge of a reasonable ISM chemo-thermal state. If we assume that a fraction of high-redshift galaxies survive until the present-day (Gnedin & Kravtsov 2006; Bovill & Ricotti 2011), then the bounds of MDFs should not exceed the ones observed in local dwarf galaxies, which typically have most of their stars within the range  $-3 < [\text{Fe}/\text{H}] < -1$  (Kirby et al. 2011). For instance in our MC simulation, the stars have a median

metallicity of  $\sim 0.3 Z_{\odot}$ , which will still exist in its MDF if we were to passively evolve them to  $z = 0$ . On the other hand, this  $M = 2 \times 10^8 M_{\odot}$  galaxy is most likely to be incorporated into a galactic bulge, based on its halo mass accretion history (Wechsler et al. 2002). However, this result of overcooling is generic to galaxies reaching  $T = 10^4$  K and should occur in dwarf galaxies that form later. Another possible way to avoid this restriction is that these stars form from a top-heavy IMF. If all of the stars form with  $M \gtrsim 0.8 M_{\odot}$ , then they will not survive until the present-day, and the MDFs from high-redshift dwarfs cannot be constrained by the observed MDFs in local dwarf galaxies.

### 5.1 Feedback prescriptions

Implementations of stellar feedback vary widely between different works. Here we discuss these variations, and their respective advantages and disadvantages. As galaxy formation simulations reach higher resolution, individual star forming clouds are being resolved. For example, Governato et al. (2010) found that a bulgeless disc galaxy forms instead of a bulge-dominated galaxy when the star formation density threshold was increased by a factor of 1000 to  $100 \text{ cm}^{-3}$ . This occurred because the simulation allowed the gas to cool and clump into smaller associations instead of a large gas reservoir at the galaxy centre. When simulations resolve these clouds, more small-scale physical processes need to be accurately modelled, and the less previous “subgrid” models are applicable because of their original assumptions of star formation on the galactic scale.

As discussed before, there are four main components to stellar feedback: photo-ionisation, photo-heating, momentum transfer from radiation, and SN explosions, in addition to stellar winds and planetary nebulae. The temporal separation of the radiative and SNe feedback is *crucial*. In the case where both mechanisms have the same time-dependency, the injection of thermal energy and heavy elements are initially dumped into a dense and cold medium, unaffected by stellar radiation. If the SNe feedback is delayed for some amount of time, in our case, the minimum lifetime of an O-star of 4 Myr, then an H II region is created surrounding the star(s), which lowers the ambient density and increases the temperature to  $\sim 10^4$  K. An optically-thick shell forms around the H II region, and radiation pressure accelerates the shell in addition to pressure forces from the H II region (Spitzer 1978). After a few Myr, the massive stars start to explode in this warm and diffuse medium, instead of a cold and dense medium. Because cooling rates are  $\propto \rho^2$ , the SN remnants are less likely to overcool in an implementation that delays SNe feedback from radiative feedback.

There have been a few types of prescriptions of SNe and momentum injection to create galactic winds and to regulate star formation. For the most part, they have an unphysical basis but replicate the observed properties of outflows and cannot study the origin of the winds.

In galaxy simulations, it has been historically difficult to resolve the multi-phase ISM. In such a simulation, SNe thermal energy is injected into a large region, usually at its resolution limit. Per timestep, the total thermal energy is only sufficient to heat the gas to  $T \sim 10^5 - 10^6$  K, where the cooling rates are maximal. If the blastwave were resolved to parsec-scales, then the temperature in the Sedov-Taylor

solution should be  $T \sim 10^8$  K, where the cooling rates are orders of magnitude lower. One approach is to neglect radiative cooling within the blastwave, allowing it to adiabatically expand (e.g. Thacker & Couchman 2000; Governato et al. 2007; Guedes et al. 2011). Using this method results in realistic late-type galaxy morphologies, but it can deviate from the observed luminosity functions because they do not suppress star formation enough, particularly in low mass galaxies, and do not drive winds at sufficiently high velocities and mass-loading factors (e.g. Guo et al. 2010). We note that another approach is to sporadically inject thermal energy only after enough SNe thermal feedback has accumulated to heat the gas to  $T \gtrsim 10^7$  K, where the cooling times are high. Here ejecta does not overcool and follows the Sedov-Taylor solution (Dalla Vecchia & Schaye 2012).

Several groups (Springel & Hernquist 2003; Oppenheimer & Davé 2008; Dalla Vecchia & Schaye 2008; Sales et al. 2010) have modelled momentum transfer from radiation by adding momentum, so-called “kicking”, to nearby particles to a velocity that is comparable to the circular velocity  $V_c$  of the halo. Similar prescriptions exist for kinetic feedback from SN explosions (Dalla Vecchia & Schaye 2008). The dependence on the choice of this kick velocity, a constant value, a constant multiple of  $V_c$ , or halo mass dependent velocity, has been shown to replicate the galaxy luminosity function and mass-metallicity relation (Finlator & Davé 2008). The kicked particles are decoupled from the hydrodynamics until they escape the virial radius. The authors acknowledge and warn that this implementation is phenomenological, and it is successful in quantifying the importance of momentum-driven winds in MW-like galaxies. Hopkins, Quataert & Murray (2011) used a more physical model for momentum loading that does not decouple the winds from the hydrodynamics and determines the momentum transfer directly from the stellar luminosity. The momentum transfer occurs within  $\lesssim 10$  pc, where they explore two schemes. Their stochastic model randomly kicks these nearby particles to the local escape velocity of the star-forming clump. Their continuous model adds the momentum  $\Delta p = (1 + \eta_p \tau_d) L/c$  at each timestep, where  $\eta_p \sim 1$  and can vary to account to uncertainties. They find that both models produce similar results. However, they do not solve the radiative transfer equation, so they must assume that the radiation is uniform within each H II region. Radiation pressure from a non-uniform distribution of massive stars may result in some cancellation of the pressure forces in the centre of the association, while still providing an overall outward force (Socrates, Davis & Ramirez-Ruiz 2008). In contrast, Krumholz & Thompson (2012) showed that the assumption of a uniform radiation field could lead to an overestimate the momentum transfer. As ionisation front instabilities grow, optically-thin gaps are created in the shock front, allowing for most of the flux to escape in these gaps and lowering the average momentum transfer per emitted photon.

Ultimately the location where momentum transfer occurs depends where the radiation is absorbed. To model this requires solving the radiative transfer equation. None of these models with the exception of Krumholz & Thompson utilises such a solver, but there are several simulation codes with coupled radiation transport. Momentum transfer from

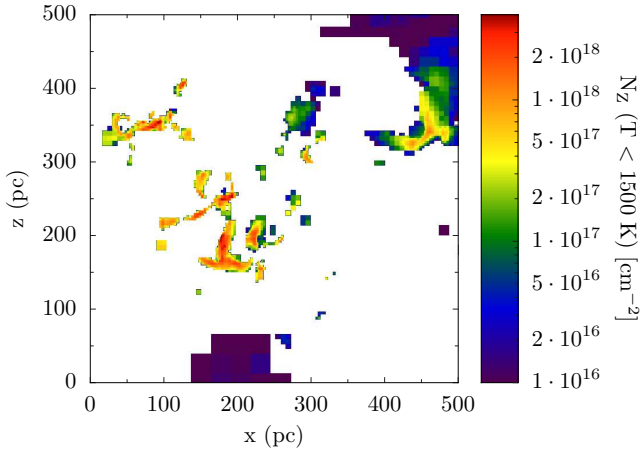


**Figure 11.** Column density of metals with  $T < 1500$  K, where dust would not be sublimated and can contribute to the opacity and enhance momentum transfer from stellar radiation. The figure is centred on the galaxy centre of mass.

ionising radiation should be straightforward to implement in these codes because the absorption coefficient is already calculated and that absorbed photon momentum should be transferred to the absorbing medium, which is how ENZO+MORAY simulates momentum loading.

## 5.2 Radiation trapping from dust and Lyman $\alpha$

In this paper, we have neglected momentum transfer from dust absorption, which then re-radiates in the IR and absorbed again many times. Thus our results represent a lower limit of star formation regulation from radiation pressure. The effective cross section of dust in the Milky Way is  $\sigma_{d,MW} \simeq 10^{-23}$  cm<sup>2</sup> per hydrogen atom in the near-IR (e.g. Draine 2003), or equivalently, an opacity  $\kappa_{d,MW} \simeq 5$  cm<sup>2</sup> g<sup>-1</sup> in terms of total gas mass. It should be noted that Rosseland dust opacity is temperature dependent, scaling as  $T^2$  below 150 K and can vary by factors of a few at  $150\text{K} < T < 1500\text{K}$ . Above 1500 K, even the most stable dust species are sublimated and the Rosseland opacity drops by a few orders of magnitude (Semenov et al. 2003). If we assume the dust extinction properties do not change with metallicity or redshift and scale the MW values with metallicity, the cross section per hydrogen atom scales with metallicity, giving  $\kappa_d = (Z/Z_\odot)\kappa_{d,MW}$ . The optical depth to dust absorption is

$$\tau_d = \int \rho \kappa_d dl = \kappa_{d,MW} \frac{\mu m_H N_Z}{Z_\odot}, \quad (18)$$

where  $N_Z$  is the column density of metals, and  $\mu$  and  $m_H$  are the mean molecular weight and mass of a hydrogen atom. We take  $Z_\odot = 0.023$  (Grevesse & Sauval 1998). Figure 11 shows the metal column density  $N_Z$  of cold ( $T < 1500$  K) gas in the inner 500 pc of the galaxy. Dust in gas  $T > 1500$  K is destroyed and is not considered in the plot. Using  $\kappa_{d,MW} = 5$  cm<sup>2</sup> g<sup>-1</sup>, the column density range  $N_Z = (10^{16}, 10^{18.6})$  cm<sup>-2</sup> corresponds to a optical depth range  $\tau_d = (10^{-5.3}, 10^{-2.7})$ . In this case, the dust absorption should have little effect on radiation momentum transfer in dwarf galaxies and only becomes significant in

MW-like galaxies. However, dust opacities may reach several hundred cm<sup>2</sup> g<sup>-1</sup> in local and distant starburst galaxies (e.g. Lehnert & Heckman 1996; Sanders & Mirabel 1996; Calzetti 2001); however, see Krumholz & Thompson (2012) for a counter-argument. In this maximal case, the optical depth  $\tau_d$  is of order unity and could boost the momentum transfer by a factor of a  $\sim$ few if the dust were to couple with the gas (e.g. Murray, Quataert & Thompson 2005).

In these low metallicity or dust-depleted cases, Lyman  $\alpha$  radiation can be trapped through resonant interactions, producing a possible significant source of radiation pressure (Henney & Arthur 1998). This process becomes insignificant when dust opacities reach unity, where dust reprocesses UV starlight into IR. Lyman  $\alpha$  radiation accumulates in the resonances, and eventually its pressure saturates, enhancing momentum transfer by a factor of

$$f_{\text{trap,Ly}\alpha} \approx 0.06 \left( \frac{\sigma_d}{\sigma_{d,MW}} \right)^{-1} \left( \frac{r}{R_{\text{eq}}} \right)^{1/2}, \quad (19)$$

where  $R_{\text{eq}}$  is the radius at where the gas pressure equals radiation pressure (Krumholz & Matzner 2009). Thus we could be further underestimating radiation pressure as Lyman  $\alpha$  trapping should become important below  $\sim 0.05 Z_\odot$ , given similar dust properties as the MW.

## 6 CONCLUSIONS

We present results from three cosmological radiation hydrodynamics simulations that demonstrate the role of radiation pressure in affecting star formation in dwarf galaxies. We progressively add more physics to our simulations to understand the impact of each process. Our reference model considers primordial chemistry and Pop II and III star formation and feedback with a transition to a Salpeter IMF at  $10^{-4} Z_\odot$ . In the next model, we add radiative cooling from metals. In our final and most realistic model, we add an H<sub>2</sub>-dissociating radiation background and momentum input from stellar radiation. Our treatment of momentum transfer from ionising radiation is accurately calculated from the optical depth given by our radiation transport module ENZO+MORAY down to our resolution limit of 1 comoving parsec. To our knowledge, this is the first cosmological galaxy simulation that has included the effects of radiation pressure that is computed from the radiative transfer equation.

The additional radiative cooling from metal species induced a runaway star formation event with a sSFR = 150 Gyr<sup>-1</sup> and SFR =  $9.9 \times 10^{-2} M_\odot \text{ yr}^{-1}$  in our most massive galaxy with  $M_{\text{DM}} = 2.0 \times 10^8 M_\odot$  at  $z = 8.1$ . This strong burst creates enough ionising photons to reionise the entire 1 Mpc<sup>3</sup> comoving domain; however, it creates a stellar population with a mean metallicity of  $0.3 Z_\odot$  that does not follow the mass-metallicity relationship of dwarf galaxies. The latter fact indicates that the galaxy is overcooling and overproducing stars. Historically, this was avoided by using higher resolution and SNe feedback, but our simulations have both of these attributes. We find that *radiation pressure plays a key role in regulating star formation* in high-redshift dwarf galaxies. The highlights of our work on the effects of radiation pressure during the formation of a dwarf galaxy are as follows.

(i) Radiation pressure alone can reduce the SFR by a factor of  $\sim 5$  to  $1.8 \times 10^{-2} M_{\odot} \text{ yr}^{-1}$ , and a similar decrease is seen in the sSFR to  $37 \text{ Gyr}^{-1}$ . About 3 per cent of the accreted gas form stars in the buildup of the stellar population.

(ii) The collision of dense shells that are driven by radiation pressure creates a turbulent medium with an rms velocity equivalent to the circular velocity of the host DM halo. This added turbulence mixes the SNe ejecta thoroughly with the entire ISM. The turbulent pressure and reduced metallicity prevents overcooling and the subsequent catastrophic collapse.

(iii) Radiation pressure in dwarf galaxies is not sufficient to launch outflows, but it provides an additional impulse to drive dense gas away from massive stars and drive interstellar turbulence. SNe energy input is still the main mechanism to drive outflows in low-mass galaxies.

(iv) Star formation regulation by radiation pressure creates a stellar population with a mean metallicity of  $10^{-2.1} Z_{\odot}$  with a normal metallicity distribution with standard deviation of 0.2 dex, agreeing with the mass-metallicity relationship of local dwarf galaxies.

(v) We show that the majority of the momentum transfer occurs in dense shells at the edges of H II regions, i.e. it is not a local process. Furthermore, the timing of numerical radiative and SNe feedback processes is critical in capturing their effects. If the SNe feedback were to be released immediately into the ISM, densities will be artificially high and the SNe input will radiate too much of its energy. In nature, H II region dynamics will evacuate the immediate volume surrounding massive stars of dense and cold gas, and SN explosions occur in a warmer, more diffuse ISM. Our simulations capture this temporal sequence, and the SN blast-waves do not overcool and are able to launch outflows from the galaxy.

(vi) The column density of metals in  $10^8 - 10^9 M_{\odot}$  dwarf galaxies reach a maximum value of  $\sim 10^{19} \text{ cm}^{-2}$ . This may imply that that momentum transfer via dust grains is not important in low-mass early galaxies.

We have shown that radiation pressure regulates star formation in dwarf galaxies in addition to photo-heating and SNe feedback. Its inclusion in galaxy formation simulations is key in forming realistic stellar populations and avoiding the overcooling problem also in high-resolution simulations that capture star forming regions with many computational elements. The impact of radiation pressure should continue to be important in larger galaxies, and we plan to apply our numerical methods to simulating such galaxies that are currently observed in the *Hubble Ultra Deep Field*.

## ACKNOWLEDGMENTS

We thank Mark Krumholz and an anonymous referee for helpful comments on this manuscript. When this work started, JHW was supported by NASA through Hubble Fellowship grant #120-6370 awarded by the Space Telescope Science Institute, which is operated by the Association of Universities for Research in Astronomy, Inc., for NASA, under contract NAS 5-26555. MJT acknowledges support by the NSF CI TraCS fellowship award OCI-1048505. Computational resources were provided by NASA/NCCS award SMD-11-2258 and a director's discretionary allocation on

SDSC Trestles. This work was partially supported by NASA ATPF grant NNX08AH26G, NSF AST-0807312, and NSF AST-1109243. This research has made use of NASA's Astrophysics Data System Bibliographic Services. The majority of the analysis and plots were done with *yt* (Turk et al. 2011).

## REFERENCES

- Abel T., Anninos P., Zhang Y., Norman M. L., 1997, *New Astronomy*, 2, 181
- Abel T., Bryan G. L., Norman M. L., 2002, *Science*, 295, 93
- Abel T., Wandelt B. D., 2002, *MNRAS*, 330, L53
- Abel T., Wise J. H., Bryan G. L., 2007, *ApJL*, 659, L87
- Aguirre A., Hernquist L., Katz N., Gardner J., Weinberg D., 2001a, *ApJL*, 556, L11
- Aguirre A., Hernquist L., Schaye J., Katz N., Weinberg D. H., Gardner J., 2001b, *ApJ*, 561, 521
- Aguirre A., Hernquist L., Schaye J., Weinberg D. H., Katz N., Gardner J., 2001c, *ApJ*, 560, 599
- Anninos P., Zhang Y., Abel T., Norman M. L., 1997, *New Astronomy*, 2, 209
- Bally J., Lada C. J., 1983, *ApJ*, 265, 824
- Benson A. J., 2010, *Physics Reports*, 495, 33
- Bergin E. A., Tafalla M., 2007, *ARA&A*, 45, 339
- Bertschinger E., 2001, *ApJS*, 137, 1
- Bouwens R. J., Illingworth G. D., Franx M., Ford H., 2008, *ApJ*, 686, 230
- Bouwens R. J. et al., 2011, *ArXiv e-prints* (1105.2038)
- Bovill M. S., Ricotti M., 2011, *ApJ*, 741, 18
- Bromm V., Yoshida N., 2011, *ARA&A*, 49, 373
- Brook C. B., Stinson G., Gibson B. K., Roškar R., Wadsley J., Quinn T., 2012, *MNRAS*, 419, 771
- Bryan G. L., Norman M. L., 1997, *ArXiv e-prints* (astro-ph/9710187)
- Bryan G. L., Norman M. L., Stone J. M., Cen R., Ostriker J. P., 1995, *Computer Physics Communications*, 89, 149
- Caffau E. et al., 2011, *Nature*, 477, 67
- Calzetti D., 2001, *PASP*, 113, 1449
- Cen R., Ostriker J. P., 1992, *ApJL*, 399, L113
- Chabrier G., 2003, *PASP*, 115, 763
- Couchman H. M. P., 1991, *ApJL*, 368, L23
- Dalla Vecchia C., Schaye J., 2008, *MNRAS*, 387, 1431
- , 2012, *ArXiv e-prints* (1203.5667)
- Danovich M., Dekel A., Hahn O., Teyssier R., 2011, *ArXiv e-prints* (1110.6209)
- Davies J. I., Alton P., Bianchi S., Trewheella M., 1998, *MNRAS*, 300, 1006
- Dekel A. et al., 2009, *Nature*, 457, 451
- Draine B. T., 2003, *ARA&A*, 41, 241
- Draine B. T., Woods D. T., 1991, *ApJ*, 383, 621
- Eddington A. S., 1926, *The Internal Constitution of the Stars*
- Efstathiou G., Davis M., White S. D. M., Frenk C. S., 1985, *ApJS*, 57, 241
- Fan X., Carilli C. L., Keating B., 2006, *ARA&A*, 44, 415
- Ferrara A., 1993, *ApJ*, 407, 157
- Ferrarese L., Merritt D., 2000, *ApJL*, 539, L9
- Finkelstein S. L., Papovich C., Giavalisco M., Reddy N. A., Ferguson H. C., Koekemoer A. M., Dickinson M., 2010, *ApJ*, 719, 1250



- Finlator K., Davé R., 2008, *MNRAS*, 385, 2181
- Franco J., 1983, *ApJ*, 264, 508
- Frebel A., Simon J. D., Geha M., Willman B., 2010, *ApJ*, 708, 560
- Gebhardt K. et al., 2000, *ApJL*, 539, L13
- Glover S. C. O., Abel T., 2008, *MNRAS*, 388, 1627
- Gnedin N. Y., 2000, *ApJ*, 542, 535
- Gnedin N. Y., Hui L., 1998, *MNRAS*, 296, 44
- Gnedin N. Y., Kravtsov A. V., 2006, *ApJ*, 645, 1054
- Górski K. M., Hivon E., Banday A. J., Wandelt B. D., Hansen F. K., Reinecke M., Bartelmann M., 2005, *ApJ*, 622, 759
- Governato F. et al., 2010, *Nature*, 463, 203
- Governato F., Willman B., Mayer L., Brooks A., Stinson G., Valenzuela O., Wadsley J., Quinn T., 2007, *MNRAS*, 374, 1479
- Grebel E. K., Gallagher, III J. S., Harbeck D., 2003, *AJ*, 125, 1926
- Greif T. H., Glover S. C. O., Bromm V., Klessen R. S., 2010, *ApJ*, 716, 510
- Greif T. H., Johnson J. L., Bromm V., Klessen R. S., 2007, *ApJ*, 670, 1
- Greif T. H., Johnson J. L., Klessen R. S., Bromm V., 2008, *MNRAS*, 387, 1021
- Grevesse N., Sauval A., 1998, *Space Science Reviews*, 85, 161, 10.1023/A:1005161325181
- Guedes J., Callegari S., Madau P., Mayer L., 2011, *ApJ*, 742, 76
- Guo Q., White S., Li C., Boylan-Kolchin M., 2010, *MNRAS*, 404, 1111
- Haehnelt M. G., 1995, *MNRAS*, 273, 249
- Heger A., Fryer C. L., Woosley S. E., Langer N., Hartmann D. H., 2003, *ApJ*, 591, 288
- Heger A., Woosley S. E., 2002, *ApJ*, 567, 532
- Henney W. J., Arthur S. J., 1998, *AJ*, 116, 322
- Hopkins P. F., Quataert E., Murray N., 2011, *MNRAS*, 417, 950
- Jubelgas M., Springel V., Enßlin T., Pfrommer C., 2008, *A&A*, 481, 33
- Karim A. et al., 2011, *ApJ*, 730, 61
- Katz N., Weinberg D. H., Hernquist L., 1996, *ApJS*, 105, 19
- Khochfar S., Silk J., 2011, *MNRAS*, 410, L42
- Kirby E. N., Lanfranchi G. A., Simon J. D., Cohen J. G., Guhathakurta P., 2011, *ApJ*, 727, 78
- Kitayama T., Yoshida N., Susa H., Umemura M., 2004, *ApJ*, 613, 631
- Komatsu E., et al., 2011, *ApJS*, 192, 18
- Kotarba H., Lesch H., Dolag K., Naab T., Johansson P. H., Donnert J., Stasyszyn F. A., 2011, *MNRAS*, 415, 3189
- Krumholz M. R., Matzner C. D., 2009, *ApJ*, 703, 1352
- Krumholz M. R., Matzner C. D., McKee C. F., 2006, *ApJ*, 653, 361
- Krumholz M. R., Thompson T. A., 2012, *ArXiv e-prints* (1203.2926)
- Lehnert M. D., Heckman T. M., 1996, *ApJ*, 472, 546
- Li Z.-Y., Shu F. H., 1996, *ApJ*, 472, 211
- Machacek M. E., Bryan G. L., Abel T., 2001, *ApJ*, 548, 509
- Madau P., Ferguson H. C., Dickinson M. E., Giavalisco M., Steidel C. C., Fruchter A., 1996, *MNRAS*, 283, 1388
- Matzner C. D., 2007, *ApJ*, 659, 1394
- Matzner C. D., McKee C. F., 1999, *ApJL*, 526, L109
- McKee C. F., Ostriker E. C., 2007, *ARA&A*, 45, 565
- McLure R. J., Dunlop J. S., Cirasuolo M., Koekemoer A. M., Sabbi E., Stark D. P., Targett T. A., Ellis R. S., 2010, *MNRAS*, 403, 960
- McLure R. J. et al., 2011, *MNRAS*, 418, 2074
- Monelli M. et al., 2010, *ApJ*, 722, 1864
- Murray N., Ménard B., Thompson T. A., 2011, *ApJ*, 735, 66
- Murray N., Quataert E., Thompson T. A., 2005, *ApJ*, 618, 569
- Nomoto K., Tominaga N., Umeda H., Kobayashi C., Maeda K., 2006, *Nuclear Physics A*, 777, 424
- Norman C., Silk J., 1980, *ApJ*, 238, 158
- Omukai K., Yoshii Y., 2003, *ApJ*, 599, 746
- Oppenheimer B. D., Davé R., 2008, *MNRAS*, 387, 577
- O'Shea B. W., Bryan G., Bordner J., Norman M. L., Abel T., Harkness R., Kritsuk A., 2004, *ArXiv e-prints* (astro-ph/0403044)
- O'Shea B. W., Norman M. L., 2007, *ApJ*, 654, 66
- , 2008, *ApJ*, 673, 14
- Osterbrock D. E., 1989, *Astrophysics of gaseous nebulae and active galactic nuclei*, Osterbrock, D. E., ed.
- Ouchi M. et al., 2010, *ApJ*, 723, 869
- Safraneck-Shrader C., Bromm V., Milosavljević M., 2010, *ApJ*, 723, 1568
- Sales L. V., Navarro J. F., Schaye J., Dalla Vecchia C., Springel V., Booth C. M., 2010, *MNRAS*, 409, 1541
- Sanders D. B., Mirabel I. F., 1996, *ARA&A*, 34, 749
- Schaerer D., 2002, *A&A*, 382, 28
- , 2003, *A&A*, 397, 527
- Schaerer D., de Barros S., 2010, *A&A*, 515, A73
- Semenov D., Henning T., Helling C., Ilgner M., Sedlmayr E., 2003, *A&A*, 410, 611
- Shapiro P. R., 1986, *PASP*, 98, 1014
- Shu F. H., Ruden S. P., Lada C. J., Lizano S., 1991, *ApJL*, 370, L31
- Smith B., Sigurdsson S., Abel T., 2008, *MNRAS*, 385, 1443
- Socrates A., Davis S. W., Ramirez-Ruiz E., 2008, *ApJ*, 687, 202
- Spitzer L., 1978, *Physical processes in the interstellar medium*, Spitzer, L., ed.
- Springel V., Hernquist L., 2003, *MNRAS*, 339, 289
- Stark D. P., Ellis R. S., Bunker A., Bundy K., Targett T., Benson A., Lacy M., 2009, *ApJ*, 697, 1493
- Tegmark M., Silk J., Rees M. J., Blanchard A., Abel T., Palla F., 1997, *ApJ*, 474, 1
- Thacker R. J., Couchman H. M. P., 2000, *ApJ*, 545, 728
- Thompson T. A., Quataert E., Murray N., 2005, *ApJ*, 630, 167
- Tolstoy E., Hill V., Tosi M., 2009, *ARA&A*, 47, 371
- Tolstoy E. et al., 2004, *ApJL*, 617, L119
- Toro E. F., Spruce M., Speares W., 1994, *Shock Waves*, 4, 25, 10.1007/BF01414629
- Tremaine S. et al., 2002, *ApJ*, 574, 740
- Trenti M., Stiavelli M., 2009, *ApJ*, 694, 879
- Truelove J. K., Klein R. L., McKee C. F., Holliman, II J. H., Howell L. H., Greenough J. A., 1997, *ApJL*, 489, L179+
- Turk M. J., Smith B. D., Oishi J. S., Skory S., Skillman S. W., Abel T., Norman M. L., 2011, *ApJS*, 192, 9
- Wang P., Abel T., 2009, *ApJ*, 696, 96

- Wechsler R. H., Bullock J. S., Primack J. R., Kravtsov A. V., Dekel A., 2002, *ApJ*, 568, 52  
Whalen D., Abel T., Norman M. L., 2004, *ApJ*, 610, 14  
Whalen D., van Veelen B., O’Shea B. W., Norman M. L., 2008, *ApJ*, 682, 49  
Wise J. H., Abel T., 2005, *ApJ*, 629, 615  
—, 2007a, *ApJ*, 665, 899  
—, 2007b, *ApJ*, 671, 1559  
—, 2008, *ApJ*, 685, 40  
—, 2011, *MNRAS*, 414, 3458  
Wise J. H., Cen R., 2009, *ApJ*, 693, 984  
Wise J. H., Turk M. J., Norman M. L., Abel T., 2012, *ApJ*, 745, 50  
Woodward P., Colella P., 1984, *Journal of Computational Physics*, 54, 115  
Woosley S. E., Weaver T. A., 1995, *ApJS*, 101, 181  
Yorke H. W., Tenorio-Tagle G., Bodenheimer P., 1983, *A&A*, 127, 313

This paper has been typeset from a  $\text{\LaTeX}$  file prepared by the author.